

A unified breaking onset criterion for surface gravity water waves in arbitrary depth

Morteza Derakhti¹, James T. Kirby², Michael L. Banner³, Stephan T. Grilli⁴ and Jim Thomson¹

¹Applied Physics Laboratory, University of Washington, Seattle, WA, USA

²Center for Applied Coastal Research, Department of Civil and Environmental Engineering, University of Delaware, Newark, DE, USA

³School of Mathematics and Statistics, University of New South Wales, Sydney, Australia

⁴Department of Ocean Engineering, University of Rhode Island, Narragansett, RI, USA

Key Points:

- The breaking onset criterion developed by *Barthelemy et al.* [2018] is shown to be applicable to waves breaking in shallow water over varying bathymetry.
- The new criterion is suitable for use in wave-resolving models that cannot intrinsically detect the onset of wave breaking.
- A comparison of model predictions based on a BEM potential flow solver and the LES/VOF model developed by *Derakhti and Kirby* [2014a] shows that the LES/VOF model provides accurate descriptions of conditions at steep wave crests.

20 **Abstract**

21 We investigate the validity and robustness of the *Barthelemy et al.* [2018] wave break-
 22 ing onset prediction framework for surface gravity water waves in arbitrary water depth, in-
 23 cluding shallow water breaking over varying bathymetry. We show that the *Barthelemy et al.*
 24 [2018] breaking onset criterion, which they validated for deep and intermediate water depths,
 25 also segregates breaking crests from non-breaking crests in shallow water, with subsequent
 26 breaking always following the exceedance of their proposed generic breaking threshold. We
 27 consider a number of representative wave types, including regular, irregular, solitary, and
 28 focused waves, shoaling over idealized bed topographies including an idealized bar geom-
 29 etry and a mildly- to steeply-sloping planar beach. Our results show that the new breaking
 30 onset criterion is capable of detecting single and multiple breaking events in time and space
 31 in arbitrary water depth. Further, we show that the new generic criterion provides improved
 32 skill for signaling imminent breaking onset, relative to the available kinematic or geometric
 33 breaking onset criteria in the literature. In particular, the new criterion is suitable for use in
 34 wave-resolving models that cannot intrinsically detect the onset of wave breaking.

35 **1 Introduction**

36 Surface wave breaking is a highly dissipative process, transferring excess wave en-
 37 ergy flux into currents and turbulence *Melville* [1996]. Familiar breaking onset manifests
 38 as a crest breaking event characterized by the formation of a multi-valued free surface and
 39 entrainment of air bubbles into the water column (excluding micro-breakers which do not
 40 entrain air). An important exception discussed below is surging breakers over very steep
 41 beaches, in which the wave crest remains relatively smooth and the initiation of instability
 42 occurs at the toe (leading edge) of the wave.

43 We introduce a new term, *breaking inception*, which identifies the critical time at which
 44 a wave crest breaking event is initiated within the growing crest region. This precedes any of
 45 the familiar visible breaking onset signatures identified above by a finite time, typically a
 46 small fraction of the local wave period. It is shown below that the breaking inception time is
 47 crucial for predicting breaking onset and breaking strength in advance of their realization.

48 Finding a robust and universal diagnostic parameter that determines the onset of break-
 49 ing for surface gravity waves, and its strength, is of substantial importance in the prediction

50 of atmosphere-ocean exchanges, nearshore circulation and mixing, design of offshore and
 51 nearshore infrastructures, etc, but as yet the problem is not completely resolved.

52 Considerable effort has been made to find a robust and universal methodology to pre-
 53 dict the onset of breaking gravity water waves in deep and intermediate depth water [Song
 54 and Banner, 2002; Wu and Nepf, 2002; Banner and Peirson, 2007; Babanin *et al.*, 2007;
 55 Tian *et al.*, 2008; Toffoli *et al.*, 2010; Shemer and Liberzon, 2014; Fedele *et al.*, 2016; Saket
 56 *et al.*, 2017, 2018; Barthelemy *et al.*, 2018; Khait and Shemer, 2018; Craciunescu and Chris-
 57 tou, 2019; Pizzo and Melville, 2019]. This and other aspects of wave breaking have been
 58 covered in several excellent reviews of the topic [Banner and Peregrine, 1993; Melville,
 59 1996; Perlin *et al.*, 2013]. Recently, Perlin *et al.* [2013] have reviewed the latest progress
 60 on prediction of geometry, breaking onset, and energy dissipation of steepness-limited break-
 61 ing waves. The predictive parameters involved can be categorized as (i) geometric, (ii) kine-
 62 matic, and (iii) dynamic criteria. As summarized in Perlin *et al.* [2013, §3], none of the
 63 available criteria can distinguish between breaking and non-breaking crests in a universal
 64 sense.

65 The situation becomes even more complex in shallow water, where waves evolve in
 66 response to interaction with seabeds of arbitrary, complex geometry. The inclusion of wa-
 67 ter depth d as an important factor in shallow water breaking leads to the identification of
 68 a convenient dimensionless parameter $\gamma = H/d$ [McCowan, 1894], where H is the local
 69 wave height. Further, analysis of breaking criteria for the simplest case of waves shoaling
 70 over a planar slope introduces the slope itself as a parameter. The effect of bottom slope m
 71 in combination with a measure of wave steepness has been studied by Iribarren and Nogales
 72 [1949], who defined a single combination $\xi_0 = m/\sqrt{H_0/L_0}$ based on offshore wave height
 73 H_0 and wavelength L_0 , and Battjes [1974], who defined a similar surf similarity parameter
 74 $\xi_b = m/\sqrt{H_b/L_b}$, with the index b denoting values taken at the time when visible breaking
 75 commences. The surf similarity parameter has been found to be useful in discriminating be-
 76 tween breaker types as well as in refining the prediction of breaking onset based on γ . The
 77 range of results in the literature is reviewed by Robertson *et al.* [2013], who list six types of
 78 dependency of γ_b on additional parameters such as m and ξ_0 , and provide a table of thirty-six
 79 examples of published formulae for the estimation of γ_b . Robertson *et al.* concluded that a
 80 single, easily implementable relationship covering all breaking phenomena is still elusive.

Our approach in this paper is underpinned by the conceptual framework paper *Barthelemy et al. [2018]* (hereafter B18) for predicting breaking onset, and its companion paper *Derakhti et al. [2018]* (hereafter D18) for predicting breaking strength. These papers report the discovery of generic predictors for breaking onset and strength for 2D and 3D modulating waves in deep and intermediate depth conditions. We seek to validate that this framework is equally valid for predicting shallow water wave breaking onset.

The local energy flux parameter \mathbf{B} introduced by B18 is defined at the wave crest region as

$$\mathbf{B} = \mathcal{F}/E|\mathbf{C}| \quad (1)$$

where $\mathcal{F} = \mathbf{U}(p + E)$ is the local flux of mechanical energy/unit volume, E is the mechanical energy/unit volume, and \mathbf{U} is the local liquid velocity. The wave crest translates with propagation speed $C = |\mathbf{C}|$, which is generally time-dependent. On the free surface, the pressure p is taken to be zero, reducing the expression for \mathbf{B} to

$$B = U/C \quad (2)$$

where U is the component of liquid velocity at the wave crest in the direction of wave propagation. Although Equation (2) appears similar to the kinematic breaking onset criterion [Perlin et al., 2013, §3.2], it represents the normalized flux of mechanical energy at the crest, and thus should be considered as a dynamical criterion. The interested reader is referred to the discussion on line 21 on p.466 of B18. In the linear approximation, B simplifies to $\gamma/2$ and the local wave steepness $S = kH/2$ (k is the wave number) in shallow and deep water respectively.

B18 explains and validates the role of the parameter B (Eq. 2) as a robust predictor of whether the crest of a steepening wave evolves to breaking, or whether it stops growing and continues to propagate without breaking. B18 shows that a wave crest will evolve to breaking if B tracked at the evolving wave crest transitions through a generic threshold B_{th} , which then sets the breaking inception time. D18 shows that the rate at which B normalized by the local wave period transitions through this generic threshold also sets the breaking strength, or total energy dissipated by the breaking event. Should B not transition through B_{th} , that crest will not evolve to breaking. Thus tracking B at the evolving crest has only two outcomes - either B fails to transition through B_{th} , in which case the crest will not evolve to breaking, or else the crest will evolve to breaking inception when B transitions through B_{th} , and will then evolve rapidly to visible breaking onset. This mirrors the physics of how breaking occurs. In

111 this case, the normalized rate of change of B at the inception time provides a generic predictor
 112 of the breaking strength [Derakhti *et al.*, 2018], but this aspect of shallow water breaking
 113 is left for a companion paper in progress.

114 Based on numerical simulation of 2D and 3D focused wave packets in deep and in-
 115 termediate depths, B18 found that a value of B_{th} in the range [0.85, 0.86] provides a robust
 116 threshold that identifies imminent breaking crest in 2D and 3D wave packets propagating in
 117 deep or intermediate uniform water depths. Subsequently, using a different modeling frame-
 118 work, D18 found consistent results for representative cases of modulated wave trains and
 119 focused packets in deep and intermediate depth water. These numerical findings for 2D and
 120 3D cases were closely supported by the laboratory experiments of *Saket et al.* [2017, 2018]
 121 which include direct wind forcing.

122 It remains to determine whether the breaking threshold framework proposed by B18,
 123 i.e., $B_{th} \approx 0.85$ as a generic threshold for predicting breaking, is also valid for waves in
 124 shallow water with relatively rapidly varying depth. Our goal is to investigate in detail to
 125 what extent the results reported by B18 and D18 for deep and intermediate water waves carry
 126 over to shallow water conditions. The utility of a predictor such as $B_{th} = 0.85$, rather than
 127 the classic $B_{th} = 1$, is its application in models that cannot directly resolve breaking and fail
 128 before waves reach $B = 1$.

129 We use a large-eddy-simulation (LES)/volume-of-fluid (VOF) model [Derakhti and
 130 Kirby, 2014a, 2016] and a 2D fully nonlinear potential flow solver using a boundary ele-
 131 ment method (FNPF-BEM) [Grilli *et al.*, 1989; Grilli and Subramanya, 1996] to simulate
 132 nonlinear wave evolution, focusing on breaking onset behavior. Simulations are conducted
 133 for a variety of scenarios including regular, irregular, solitary, and focused waves shoaling
 134 over idealized bed topographies, including an idealized bar geometry and mildly- to steeply-
 135 sloping planar beaches. Additionally, we examine the applicability of the criterion for col-
 136 lapsing/surging breaking cases in shallow water, for which an instability leading to breaking
 137 may develop close to the toe (leading edge) of the wave front.

138 2 Computational approaches

139 In this section, we provide a brief overview of the two modeling approaches used: the
 140 polydisperse two-fluid LES/VOF model of *Derakhti and Kirby* [2014a] based on the model
 141 TRUCHAS [Francois *et al.*, 2006], and the FNPF-BEM model of *Grilli et al.* [1989] and

142 *Grilli and Subramanya* [1996]. The cases considered here are essentially 2D in the (x, z)
 143 plane, allowing us to employ a purely 2D version of FNPF-BEM. The FNPF-BEM model
 144 is not valid beyond the first onset of breaking, and is thus only used below to consider the
 145 transient solitary wave cases.

146 As mentioned, the focus of this study is the examination of geometry, kinematics and
 147 dynamics of an evolving crest up to the close vicinity of the visible breaking onset stage that
 148 is essentially before the start of the bubble entrainment process. However, in all simulation
 149 cases considered here, except the transient solitary wave cases, it is of interest to examine
 150 how an evolving crest interacts with decaying turbulence patches left behind from precedent
 151 breaking events. In addition, the LES/VOF model results are used for the examination of the
 152 wave-breaking-induced energy dissipation in a companion study. For these reasons, a rela-
 153 tively accurate post-breaking behavior of the simulation cases is needed, which then justifies
 154 the inclusion of bubble dynamics into our LES/VOF simulations.

155 Validation of the models for the present application is discussed in Appendix B.

156 2.1 The LES/VOF model

157 The LES/VOF computations are performed using the Navier-Stokes solver TRUCHAS
 158 [Francois *et al.*, 2006] with extensions of a polydisperse bubble phase and various turbulence
 159 models [Carrica *et al.*, 1999; Ma *et al.*, 2011; Derakhti and Kirby, 2014a]. Details of the
 160 current mathematical formulations and numerical methods may be found in *Derakhti and*
 161 *Kirby* [2014a, §2].

162 The filtered governing equations for conservation of mass and momentum of the liquid
 163 phase are given by:

$$\frac{\partial \alpha \rho}{\partial t} + \frac{\partial \alpha \rho \tilde{u}_j}{\partial x_j} = 0, \quad (3)$$

$$\frac{\partial \alpha \rho \tilde{u}_i}{\partial t} + \frac{\partial \alpha \rho \tilde{u}_i \tilde{u}_j}{\partial x_j} = \frac{\partial \Pi_{ij}}{\partial x_j} + \alpha \rho g \delta_{3i} + \mathbf{M}^{gl}, \quad (4)$$

164 where $(i, j) = 1, 2, 3$; ρ is a constant liquid density; α and \tilde{u}_i are the volume fraction and
 165 the filtered velocity in the i direction of the liquid phase, respectively; δ_{ij} is the Kronecker
 166 delta function; g is the gravitational acceleration; and $\Pi_{ij} = \alpha(-\tilde{p} \delta_{ij} + \tilde{\sigma}_{ij} - \tau_{ij})$ with \tilde{p}
 167 the filtered pressure, which is identical in each phase due to the neglect of interfacial surface
 168 tension, $\tilde{\sigma}_{ij}$ viscous stress and τ_{ij} the subgrid-scale (SGS) stress estimated using an eddy
 169 viscosity assumption and the Dynamic Smagorinsky model, which includes water/bubble

170 interaction effects [for more details see *Derakhti and Kirby*, 2014a, §2.4]. Finally, \mathbf{M}^{gl} are
 171 the momentum transfers between liquid and gas phases, including the filtered virtual mass,
 172 lift, and drag forces [*Derakhti and Kirby*, 2014a, §2.2].

173 Using the same filtering process as in the liquid phase, the equations for the bubble
 174 number density and continuity of momentum for each bubble size class with a diameter d_k^b ,
 175 $k = 1, \dots, N_G$, are then given by [*Derakhti and Kirby*, 2014a, §2]:

$$\frac{\partial N_k^b}{\partial t} + \frac{\partial \tilde{u}_{k,j}^b N_k^b}{\partial x_j} = R_k^b, \quad (5)$$

$$0 = -\frac{\partial \alpha_k^b \tilde{p}}{\partial x_j} \delta_{ij} + \alpha_k^b \rho^b g_i + \mathbf{M}_k^{lg}, \quad (6)$$

176 where $\alpha_k^b = m_k^b N_k^b / \rho^b$, m_k^b , N_k^b and $\tilde{u}_{k,j}^b$ are the volume fraction, mass, number density and
 177 filtered velocity in the j direction of the k th bubble size class; ρ^b is the bubble density; and
 178 R_k^b includes the source due to air entrainment in the interfacial cells [*Derakhti and Kirby*,
 179 2014a, §2.3], intergroup mass transfer, and SGS diffusion terms. Finally, \mathbf{M}_k^{lg} represents the
 180 total momentum transfer between liquid and the k th bubble size class, and satisfies $\mathbf{M}^{gl} +$
 181 $\sum_{k=1}^{N_G} \mathbf{M}_k^{lg} = 0$. In (6), we neglect the inertia and shear stress terms in the gas phase following
 182 *Carrica et al.* [1999] and *Derakhti and Kirby* [2014a].

183 2.2 The FNPF-BEM model

184 Equations for the 2D FNPF-BEM model are briefly presented here. The velocity po-
 185 tential $\phi(\mathbf{x}, t)$ is used to describe inviscid, irrotational flow in the vertical plane (x, z) , with
 186 the velocity defined by $\mathbf{u} = \nabla \phi = (u, w)$. ϕ is governed by Laplace's equation in the liquid
 187 domain $\Omega(t)$ with boundary $\Gamma(t)$,

$$\nabla^2 \phi = 0; \quad (x, z) \in \Omega(t) \quad (7)$$

188 Using the 2D free space Green's function, $G(\mathbf{x}, \mathbf{x}_l) = -(1/2\pi) \log |\mathbf{x} - \mathbf{x}_l|$, and Green's
 189 second identity, (7) is transformed into the boundary integral equation

$$\alpha(\mathbf{x}_l) \phi(\mathbf{x}_l) = \int_{\Gamma(\mathbf{x})} \left[\frac{\partial \phi}{\partial n}(\mathbf{x}) G(\mathbf{x}, \mathbf{x}_l) - \phi(\mathbf{x}) \frac{\partial G(\mathbf{x}, \mathbf{x}_l)}{\partial n} \right] d\Gamma(\mathbf{x}) \quad (8)$$

190 where $\mathbf{x} = (x, z)$ and $\mathbf{x}_l = (x_l, z_l)$ are position vectors for points on the boundary, \mathbf{n} is the
 191 unit outward normal vector, and $\alpha(\mathbf{x}_l)$ is a geometric coefficient. Details of the surface and
 192 bottom boundary conditions and numerical methods may be found in *Grilli et al.* [1989] and
 193 *Grilli and Subramanya* [1996]. The model provides instantaneous surface elevation and liq-
 194 uid velocity at the surface.

195 **3 Model configuration and test cases**196 **3.1 Test cases**

197 Our numerical experiments are performed in a virtual wave tank with three different
 198 idealized bed geometries, illustrated in Figure 1. Cases include deep to shallow water trans-
 199 sition conditions. We define the coordinate system (x, y, z) such that x and y represent the
 200 along-tank and transverse directions respectively and z is the vertical direction, positive up-
 201 ward and measured from the still water level. We note that waves are usually breaking over
 202 the bar crest or the down-wave slope for cases of shoaling over a bar ($x > 0$ in Figure 1b).

203 All model simulations are performed with the model initialized with quiescent condi-
 204 tions. In the LES/VOF model, we specify the total instantaneous free surface, η_w , and liquid
 205 velocity, (u_w, w_w) , at the model upstream boundary, (x_w, y, z) , for various incident wave con-
 206 ditions, including regular sinusoidal, focused packets, modulated wave trains, and irregular
 207 waves propagating over a flat bed or over a bar geometry, as well as regular cnoidal waves
 208 shoaling over a plane beach. In the BEM model, we specify solitary waves as initial condi-
 209 tion on the free surface, using the elevation, potential and normal velocity derived from the
 210 *Tanaka* [1986] solution. Table 1 summarizes the input parameters for all simulated cases.

211 In all simulated cases, the selected grid size in the x direction, Δx , is smaller than
 212 $1/100$ of the wavelength in the vicinity of the initial breaking point or unbroken crest max-
 213 imum. A uniform grid of $\Delta y = \Delta z = \Delta x/2$ is used for the simulated LES/VOF cases, with
 214 the total number of grid points varies between 0.5×10^6 and 3×10^6 . The CPU run-time of
 215 the LES/VOF simulations is typically less than a day for a 100s simulation time using 200
 216 processors on an HPC cluster.

217 **3.1.1 Focused wave packets**

218 The input focused wave packet was composed of $N = 32$ sinusoidal components of
 219 steepness $a_n k_n, n = 1, \dots, N$, where a_n and k_n are the amplitude and wave number of the n th
 220 frequency component. The steepness of individual wave components is taken to be constant
 221 across the spectrum, or $a_1 k_1 = a_i k_i = \dots = a_N k_N = S_g/N$ with $S_g = \sum_{n=1}^N a_n k_n$ taken
 222 to be a measure of the wave train global steepness. Based on linear theory, the free surface
 223 elevation at the wavemaker for 2D wave packets focusing at $x = x_f$ is given by [Rapp and

Table 1: Input parameters for the simulated cases. Each case identifier has 3 parts indicating the geometry of the wave tank (P: planar beach, B: barred beach, F: flat bed; numbers: various geometry parameters), the type of the incident waves (r: regular, i: irregular, s: solitary waves, f: focused packets, m: modulated wave trains), and the numerical model (LV: LES/VOF, BM: FNPF-BEM) respectively. Here, H_w and T_w are the wave height and period of the regular waves at the wavemaker, and $\xi_0 = s^{-1}/\sqrt{H_0/L_0}$ is the surf-similarity parameter [Battjes, 1974]; the rest of the variables are defined in Figure A.1.

Case	H_w (mm) (or S_g)	T_w (s)	d_1 (m)	L_1 (m)	s	ξ_0 (or $\Delta f/f_c$)	d_2 (m)	L_2 (m)	s_d
P1-r-LV	80, 120, 180, 200, 240	4.0	0.5	0	5	3.9 - 2.3	-	-	-
P2-r-LV	150	4.0	0.5	0	10	1.43	-	-	-
P3-r-LV	40, 150	4.0	0.5	0	20	1.38, 0.71	-	-	-
P4-r-LV	90, 150, 200	4.0	0.5	0	40	0.46 - 0.31	-	-	-
P5-r-LV	90, 150	4.0	0.5	0	100	0.18, 0.14	-	-	-
P6-r-LV	90, 120, 150	4.0	0.3	0	200	0.09 - 0.07	-	-	-
P7-s-LV	240, 260, 270, 350, 500	-	1.0	6.0	8	-	-	-	-
P7-s-BM	240	-	1.0	20.0	8	-	-	-	-
P8-s-BM	300, 450, 600	-	1.0	20.0	15	-	-	-	-
P9-s-BM	200, 600	-	1.0	20.0	100	-	-	-	-
B1-r-LV	41, 43, 46, 46.2, 46.3, 46.5, 47, 50, 53, 59	1.01	0.4	6	20	0.30 - 0.25	0.1	2	10
B2-r-LV	47, 50, 53, 59	1.01	0.4	6	100	0.06 - 0.05	0.1	2	10
B3-r-LV	24, 26, 26.5, 27, 27.5, 30, 34, 40	2.525	0.4	6	20	1.05 - 0.81	0.1	2	10
B4-r-LV	26, 30, 30.5, 31 32, 34, 40	2.525	0.4	6	100	0.21 - 0.16	0.1	2	10
B5-f-LV	(0.20, 0.21, 0.22, 0.23, 0.30)	$T_c : 1.14$	0.6	3	20	(0.75)	0.2	3	10
B6-i-LV	$H_{rms} : 40$	$T_p : 1.7$	0.47	0	20	0.52	0.12	2	10
B7-i-LV	$H_{rms} : 40$	$T_p : 1.7$	0.47	0	20	0.52	0.17	2	10
B8-s-BM	36, 40, 46, 46.6 47, 60, 80	-	0.4	8	20	-	0.1	2	10
F1-f-LV	(0.25, 0.3, 0.302, 0.31, 0.32, 0.42, 0.44, 0.46)	$T_c : 1.14$	0.6	16	-	(0.75)	-	-	-
F2-f-LV	(0.32, 0.36, 0.40)	$T_c : 1.33$	0.6	22	-	(1.0)	-	-	-
F3-m-LV	(0.160, 0.176)	$T_c : 0.68$	0.55	64	-	(0.0954)	-	-	-

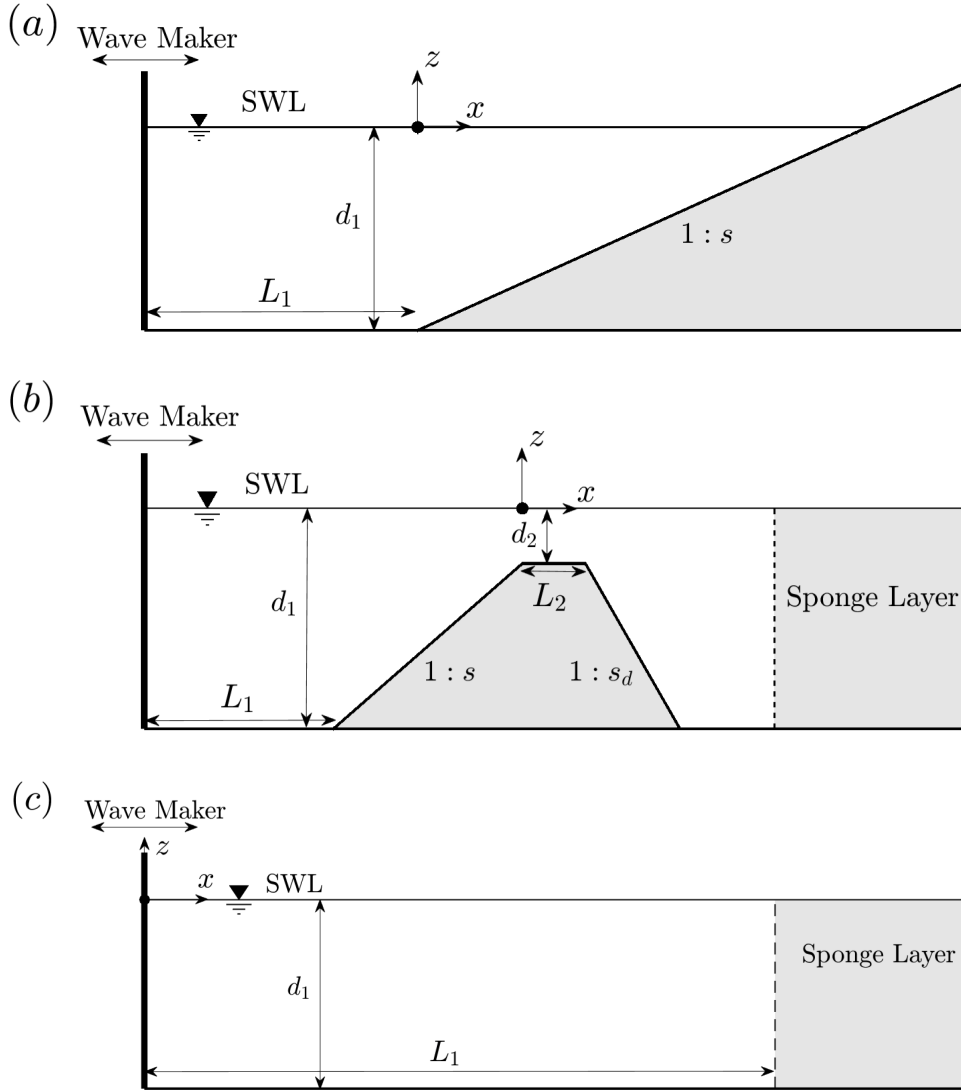


Figure 1: Schematic of the side-view of the computational domain for the waves propagating over (a) a plane beach, (b) an idealized bar, and (c) a flat bed geometry.

224 *Melville, 1990; Derakhti and Kirby, 2014a]*

$$\eta_w = \sum_{n=1}^N a_n \cos[2\pi f_n(t - t_f) + k_n(x_f - x_w)] \quad (9)$$

225 where f_n is the frequency of the n th component, x_f and t_f are the predefined, linear theory
 226 estimates of location and time of the focal point respectively. The discrete frequencies f_n
 227 are uniformly spaced over the band $\Delta f = f_N - f_1$ with the central frequency defined by
 228 $f_c = 1/2(f_N + f_1)$.

229 **3.1.2 Modulated wave trains**

230 For cases of modulated wave trains, we use the bimodal wave approach of *Banner and*
 231 *Peirson* [2007], with free surface elevation at the wavemaker given by

$$\eta_w = a_1 \cos(\omega_1 t) + a_2 \cos(\omega_2 t - \frac{\pi}{18}), \quad (10)$$

232 where $\omega_1 = 2\pi f_1$, $\omega_2 = \omega_1 + 2\pi\Delta f$, $S_g = a_1 k_1 + k_2 a_2$ and $a_2/a_1 = 0.3$. Increasing the global
 233 steepness S_g increases the strength of the resulting breaking event in both focused packets
 234 and modulated wave trains.

235 **3.1.3 Irregular wave trains**

236 For irregular wave cases, η_w is prescribed using the first $N = 2500$ Fourier components
 237 of the measured free surface time series at the most offshore gauge of the cases experimen-
 238 tally studied by *Mase and Kirby* [1992] with $T_p = 1.7$ s, given by

$$\eta_w = \sum_{n=1}^N a_n \cos(\omega_n t + \epsilon_n) \quad (11)$$

239 where a_n and ϵ_n are the amplitude and phase of the n th Fourier component based on the
 240 measured free surface time series, and ω_n is the angular frequency of the n th Fourier com-
 241 ponent. *Mase and Kirby* [1992] specified wavemaker conditions for irregular waves based
 242 on a Pierson-Moskowitz spectrum. Waves then propagated shoreward over a sloping planar
 243 beach. Here the same incident waves are used but shoal over an idealized bar. Liquid veloc-
 244 ities for each spectral component are calculated using linear theory and then superimposed
 245 linearly at the wavemaker. No correction for second order effects was made.

246 **3.1.4 Regular weakly dispersive, nonlinear waves**

247 For cnoidal waves, we use the theoretical relations for η_w and (u_w, w_w) as given in
 248 *Wiegel* [1960]. Initial conditions for solitary wave tests were specified using the solution for
 249 finite amplitude waves due to *Tanaka* [1986]. This initial condition represents a very accu-
 250 rate numerical solution to the full Euler equations, and is more suitable for use here with the
 251 fully nonlinear numerical codes being used than the standard first-order Boussinesq solitary
 252 wave solution [*e.g. Grilli and Subramanya, 1996*].

253 **3.2 Definition of a breaking crest**

254 The visible manifestation of surface wave breaking events, excluding micro-breakers, is
 255 the formation of a multi-valued free surface, which is accompanied by the initiation of wave-
 256 breaking-induced energy dissipation and entrainment of air bubbles into the water column.
 257 In most wave breaking modes, the breaking process initiates visibly at the crest of the break-
 258 ing wave. Exceptions include surging breakers over very steep beaches in which the crest of
 259 the wave remains relatively smooth and the initiation of instability occurs at the toe (leading
 260 edge) of the wave.

261 Here, we consider an individual evolving crest to be a breaking crest if the initiation
 262 of multi-valued free surface occurs in the crest region, e.g., developing a vertical tangent on
 263 the forward face of the crest, followed rapidly by a spilling or plunging plume surging from
 264 the crest down the forward face. In all breaking crests considered here, the onset of breaking
 265 occurs fairly rapidly after a vertical tangent becomes apparent onshore of the crest.

266 In the BEM framework, there is no dissipation mechanism in the model, and the model
 267 becomes unstable fairly rapidly after a vertical tangent becomes apparent at or near the crest,
 268 and a breaker jet starts forming. Thus, as was proposed in earlier work [e.g., *Grilli et al.*,
 269 1997], an individual crest in simulations using the FNPF-BEM model is also denoted as a
 270 breaking crest when the free surface slope at any given point on the front face of the wave
 271 (i.e., onshore of the crest) becomes vertical; a multi-valued free surface elevation will typi-
 272 cally occur at the next time step of computations.

273 **4 Results**

274 In this section, we examine in detail the onset of breaking on basis of the parameter
 275 $B = U/C$ (Eq. 2) for representative breaking and non-breaking incident waves in interme-
 276 diate depth and shallow water. The results for steepness-limited wave breaking in both fo-
 277 cused packets and modulated wave trains [*Derakhti et al.*, 2018] are also presented. In the
 278 following section (§5.2), we show that several geometric criteria for predicting the onset of
 279 breaking are not uniformly robust.

280 Frames (a), (d), and (g) of Figure 2 show examples of the computed temporal variation
 281 of C from shallow to deep water, in which values of C are normalized by their corresponding
 282 values at the time $t^* = 0$ marking either the time when $B = 0.85$ or, for non-breaking cases,
 283 the occurrence of maximum crest elevation. In this and subsequent plots, the color black for

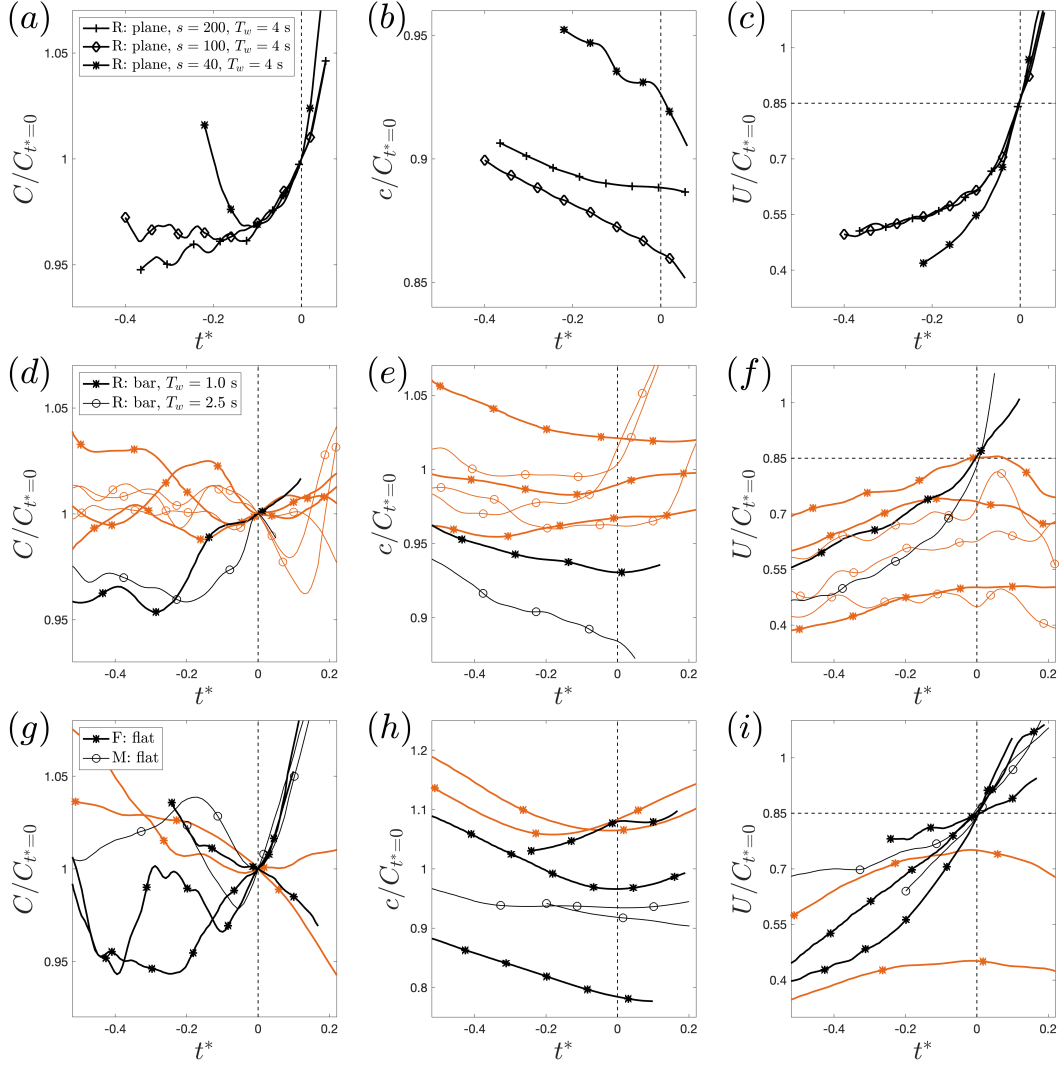


Figure 2: Examples of the temporal variation of (a, d, g) the crest propagation speed C , (b, e, h) phase speed $c = \sqrt{gk^{-1} \tanh [k(d + H_c)]}$, and (c, f, i) the horizontal particle velocity at the crest U , all normalized by the corresponding C value at $t^* = 0$, for breaking (black symbols and lines) and non-breaking (orange symbols and lines) crests in (a, b, c): regular waves (R) shoaling over a plane beach with slope $m = 1/s$, (d, e, f): regular waves (R) propagating over a bar, and (g, h, i): focused packets (F) and modulated wave trains (M) in deep and intermediate water.

284 curves or points indicates cases where breaking occurs, while orange indicates non-breaking
 285 cases. Frames (b), (e), and (h) show results for an estimate of phase speed c based on an ap-
 286 proximate nonlinear dispersion relation $c = \sqrt{gk^{-1} \tanh[k(d + H_c)]}$ which is slightly differ-
 287 ent than that proposed by *Booij* [1981] (replacing $H/2$ by the crest height H_c). The behavior
 288 of crest translation speed C is seen to be distinctly different from estimates based on disper-
 289 sion relations for regular waves. The results show that the ratio c/C around $t^* = 0$ ranges
 290 between 0.8 and 1.1 in most cases.

291 We note that C is obtained by calculating the rate of change of the horizontal location
 292 of an evolving crest, e.g., x_{η_c} if the crest is propagating in the x direction. In both BEM and
 293 LES/VOF frameworks, x_{η_c} may occur between the grid locations, and thus a local fitting
 294 (or smoothing) to the predicted free surface locations ($\eta(x, y, t)$) is needed to obtain a robust
 295 estimate of x_{η_c} for each evolving crest. Such local fitting (or smoothing) also removes the
 296 potential noise in the calculated C values due to the existence of local maxima in the crest
 297 region due to the presence of relatively high frequency waves, especially when they are prop-
 298 agating in the direction opposite to that of the dominant wave. Although implementing local
 299 fitting (or smoothing) for predicted maximum η values and their locations significantly im-
 300 proves the estimation of C , in some cases there are still some small undulations in the C val-
 301 ues (as shown in the left column of Figure 2) obtained from tracking the location of η_c (e.g.,
 302 $C = dx_{\eta_c}/dt$). For unsteadily evolving dispersive wave packets, the generic crest slowdown
 303 mechanism results in a systematic variability in C [see for example *Banner et al.*, 2014, for
 304 more details].

305 In addition, the estimation of C will be challenging in cases in which the crest region is
 306 relatively flat. One clear example of such cases is the time at which an evolving crest reaches
 307 the shoreline and the wave rapidly surges up-slope without overturning; such cases are de-
 308 tailed later in the text. Considering these uncertainties, we can write $C = C_e \pm \Delta C$ where
 309 C_e is the exact propagation speed of the evolving crest and ΔC represents the corresponding
 310 uncertainty estimate. The results of the temporal variation of C (e.g., Figure 2a,d,g) suggest
 311 that $\Delta C/C_e < 0.01$ prior to $t^* = 0$ in the simulated cases in which the crest region has a
 312 resolved curvature in the considered discretization.

313 In the BEM model, U is the actual particle velocity on the free surface at the wave
 314 crest. In the LES/VOF model, we set U as the maximum of the computed horizontal near-
 315 surface velocity over the computational cells in the range $x_{\eta_c} \pm 3\Delta x$. We also perform a

simple smoothing, using the moving average method, on the U time series for each evolving crest before calculating B values. Frames (c), (f), and (i) of Figure 2 show examples of the temporal evolution of U normalized by their corresponding C values at the time $t^* = 0$, $C_{t^*=0}$. In Figure 2, all C , c , and U values that correspond to an evolving crest are normalized by a single value $C_{t^*=0}$, the propagation speed of the crest at the time $t^* = 0$. Thus $U/C_{t^*=0}$ is not equal to B for $t^* \neq 0$. Our results show that U significantly increases as an evolving crest approaches the break point $t^* = t_b^*$ (which typically occurs in the range $[0, 0.2]$), as opposed to C , which varies by less than 5% in the range $-0.4 < t^* < t_b^*$ for cases of shoaling over gentle to moderate slopes or cases in deep and intermediate depth water. For these cases, the results suggest that the variation in B is mainly related to variation in U in the range $-0.4 < t^* < t_b^*$.

We also write U in terms of the exact value (U_e) and an uncertainty estimate (ΔU), $U = U_e \pm \Delta U$, in which the results indicate that $\Delta U/U_e < \Delta C/C_e$ for most cases. Thus, we can write

$$B = \frac{U_e \pm \Delta U}{C_e \pm \Delta C} = \frac{U_e}{C_e} \times \frac{1 \pm \Delta U/U_e}{1 \pm \Delta C/C_e} = B_e(1 \pm \Delta U/U_e)\left(1 \pm \Delta C/2C_e + O([\Delta C/C_e]^2)\right). \quad (12)$$

where B_e represents the exact value of B , and then the uncertainty in the estimated B values, denoted by ΔB , reads in relative value as

$$\pm \Delta B/B_e = \pm \Delta U/U_e \pm \Delta C/2C_e + O([\Delta C/C_e]^2, [\Delta C/C_e][\Delta U/U_e]). \quad (13)$$

Based on these results and taking $\Delta U/U_e < \Delta C/C_e < 0.01$, the uncertainty in the estimated B values from our numerical experiments (describe below) will be $\Delta B/B_e < 0.015$ for the cases in which the crest region has a resolved curvature in the considered discretization. In particular, $\Delta B < 0.013$ for B values approaching the breaking inception threshold value B_{th} , which varied in the range $[0.85, 0.86]$ in the numerical cases of B18. Further, *Saket et al.* [2017, 2018] reported an uncertainty estimation of $\Delta B = 0.020$ for their experimental measurements.

4.1 Results for waves shoaling over a plane beach

Figure 3 shows examples of the evolution of regular waves (with $T_w = 4$ s) over a plane beach with a slope $m = 1/s$; including shoaling, breaking onset and progression of breaking crests; and the corresponding temporal variation of the breaking onset parameter B for the tracked crests. The incident waves cover a wide range of ξ_0 values, demonstrating a transition

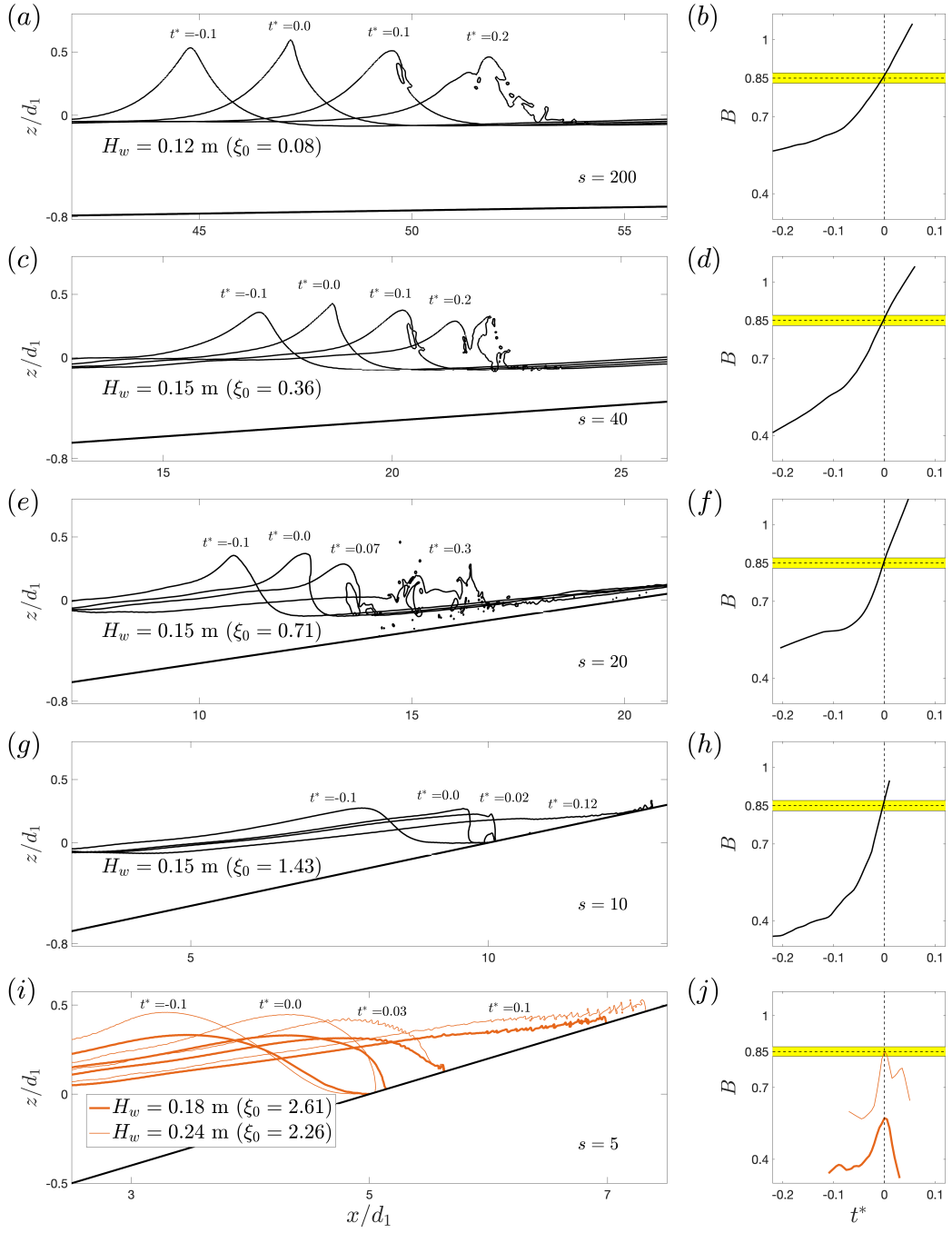


Figure 3: (a, c, e, g, i): Snapshots of free surface elevations and (b, d, f, h, j): temporal evolution of the breaking onset parameter B for regular waves ($T_w = 4 \text{ s}$) propagating over a plane beach with a slope $m = 1/s$, demonstrating a transition from spilling to collapsing and surging breaking with an increasing $\xi_0 = s^{-1}/\sqrt{H_0/L_0}$ (see Table 1). Here d_1 is the still water depth at the beginning of the plane slope segment (Figure 1a). Cases without an apparent overturning crest are indicated in orange. All results are obtained using the LES/VOF model. The yellow regions indicate $B = 0.85 \pm 0.02$.

344 from spilling breaking, frames (a-b), to collapsing and surging breaking, frames (g-j). We
 345 observe that B always transitions through the breaking inception threshold value $B_{th} \approx 0.85$
 346 prior to visible crest breaking in cases in which breaking is due to the initiation of instability
 347 in the crest region (i.e., spilling or plunging breakers). In these cases, we also observe that
 348 B exceeds 1 shortly after the breaking inception threshold value $B_{th} \approx 0.85$ is transitioned,
 349 and the time scale $\Delta t_{onset} = t_{B=1} - t_{B=B_{th}}$ is a decreasing function of ξ_0 for breaking waves
 350 with the same wave period (T_w here). Note that in shorebreaks, Δt_{onset} is relatively small
 351 and estimating B is challenging due to rapid changes, uncertainty, and ambiguity in defining
 352 x_{η_c} after $B = B_{th}$ is transitioned. For example, in the shorebreak case shown in frames (g-h),
 353 the calculation of B is terminated before reaching $B = 1$ due to a poor estimation of C as the
 354 wave transitions through the time at which $B = B_{th}$. Frames (i) and (j) show the results for
 355 two cases with $\xi_0 = 2.26$ and 2.61 surging over a slope of $1/5$ or slope angle 11.31° . In both
 356 cases, the initiation of instability occurs at the toe of the wave, and the maximum B values
 357 remain below B_{th} .

358 Figure 4 shows similar results to those of Figure 3 for solitary wave cases shoaling over
 359 steep beaches simulated using the BEM (dashed lines) and LES/VOF (solid lines) models.
 360 Here and subsequently, dashed and solid lines represent results of simulations using the BEM
 361 and LES/VOF models, respectively. Breaking of solitary waves on plane slopes from $1/100$
 362 to $1/8$ was studied using the BEM model by *Grilli et al.* [1997], who reported no breaking
 363 for slopes greater than 12° . Using a least-square error method based on their numerical ex-
 364 periments, *Grilli et al.* [1997] proposed a maximum limit for non-breaking solitary waves
 365 shoaling on a slope $m = 1/s$ given by $H_w^m = 16.9d_1/s^2$. They also introduced a parame-
 366 ter $\zeta_0 = 1.521/s\sqrt{H_w/d_1}$ and characterized the type of their breaking cases based on ζ_0 as
 367 surging when $0.30 < \zeta_0 < 0.37$, plunging when $0.025 < \zeta_0 < 0.30$, and spilling when
 368 $\zeta_0 < 0.025$.

369 Figure 4a shows the BEM model results for the evolution of a plunging breaking soli-
 370 tary wave on a slope $1/15$ with $H_w = 0.30$ m $> H_w^m = 0.08$ m and $\zeta_0 = 0.19$ ($d_1 = 1$
 371 m). Frames (c) and (e) show results of the LES/VOF model for two cases on a slope $1/8$
 372 ($H_w^m = 0.264$) with $H_w = 0.50$ m ($\zeta_0 = 0.27$) and $H_w = 0.35$ ($\zeta_0 = 0.32$). For all three
 373 cases shown in frames (a-f), the occurrence and breaking type of the incident solitary waves
 374 predicted by both the BEM and LES/VOF models are consistent with the predictions from
 375 H_w^m and ζ_0 [*Grilli et al.*, 1997]. In all three cases, we observe that the corresponding B pa-
 376 rameter reaches 0.85 close to a time at which a vertical tangent appears on the crest front

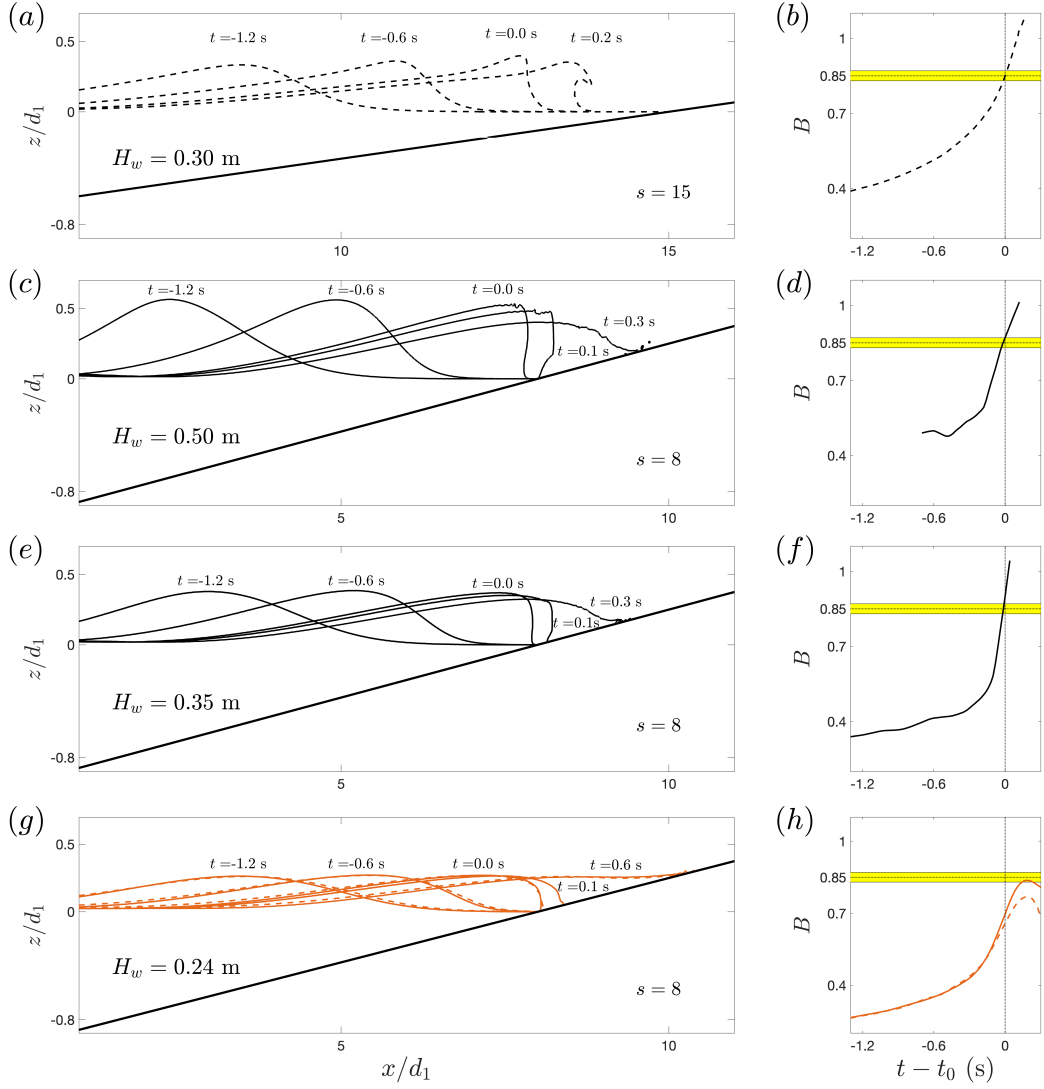


Figure 4: (a, c, e, g): Snapshots of the free surface elevations and (b, d, f, h): the temporal evolution of the breaking onset parameter B for solitary waves propagating over a plane beach with a slope $m = 1/s$. Dashed and solid lines represent the results for cases simulated using the BEM and LES/VOF models respectively. The yellow regions indicate $B = 0.85 \pm 0.02$.

377 face. As in Figure 3, we also observe that B exceeds 1 shortly after B_{th} is transitioned for all
 378 breaking solitary waves, and the time scale $\Delta t_{onset} = t_{B=1} - t_{B=B_{th}}$ is a decreasing function
 379 of ζ_0 , consistent with the trend observed for regular waves with respect to ξ_0 (Figure 3).

380 Figure 4g shows the evolution of a non-breaking solitary wave on a slope 1/8 with
 381 $H_w = 0.24 \text{ m} < H_w^m = 0.264 \text{ m}$ predicted by both the BEM and LES/VOF models. Frame
 382 (h) shows the calculated B curves from both model results. In this case, t_0 represents the time
 383 of occurrence of maximum crest elevation, as opposed to Frames (a-f) in which t_0 represents
 384 the time when $B = 0.85$. The maximum B values, B_m , from both models remain below B_{th} ;
 385 however, B_m calculated from the BEM model, is approximately 6% smaller than that from
 386 the LES/VOF model results.

387 Figure 5 shows the temporal variations of x_{η_c} , C and U predicted by both models. The
 388 maximum difference between C and U values predicted by each model is approximately 4%.
 389 Before the time at which the crest maximum is reached ($t < t_0$), U from the BEM model
 390 is almost the same as that predicted by the LES/VOF model except close to the crest maxi-
 391 mum time, where the difference between the two predictions reaches 1%. The BEM model
 392 prediction for C is smaller and greater than that predicted by the LES/VOF model for $t < t_0$
 393 and $t > t_0$, indicating that the BEM-predicted wave crest is pitching forward somewhat more
 394 slowly than the LES/VOF-predicted crest. The discrepancy in the corresponding B values
 395 is a maximum after $t > t_0$, with a value of $\approx 6\%$. The discrepancy between the BEM and
 396 LES/VOF results is partly due to their different spatial resolution ($\Delta x_{BEM} \approx 13\Delta x_{LES/VOF}$)
 397 and the neglect of bed friction and viscous effects in the BEM model. Further, a part of the
 398 discrepancy is related to the uncertainty in the estimation of C as the crest region becomes
 399 relatively flat, particularly for surging/shorebreak cases. Overall, we find that the two model-
 400 ing approaches provide consistent estimates of liquid velocity and crest geometry evolution
 401 in cases where adequate spatial and temporal resolutions are used. This conclusion is further
 402 supported by the general consistency observed between intermediate and deep water results
 403 in the studies of B18 and D18, and contrasts with the negative evaluation of the LES/VOF
 404 approach made in *Pizzo and Melville* [2019]. This is further supported by validations pre-
 405 sented in the Appendix B.

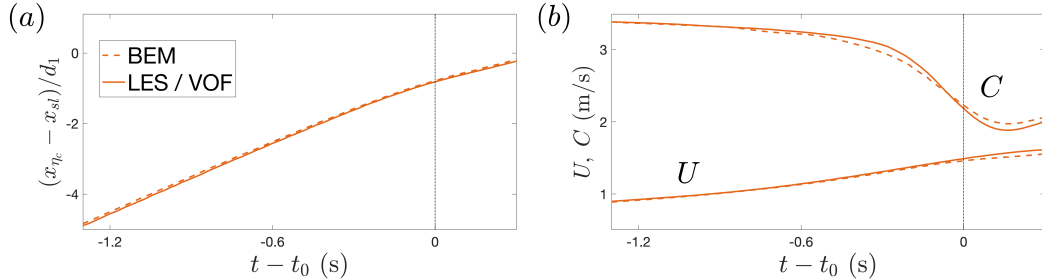


Figure 5: Temporal evolution of (a) x_{η_c} the horizontal location of the crest, and (b) C crest propagation speed and U particle horizontal velocity at the crest for the non-breaking solitary wave shown in Figure 4g. Dashed and solid lines show results of simulations cases with the BEM and LES/VOF models, respectively. Here x_{sl} is the cross-shore location of the shoreline.

4.2 Results for waves shoaling over an idealized bar

As mentioned in the introduction section, the breaking inception threshold value $B_{th} \approx 0.85$ may be considered as the indicator of breaking onset, with any wave for which B exceeds B_{th} inevitably breaking visibly a short time (Δt_{onset}) later. However, one still needs to closely examine the behavior of B in the transition from breaking to non-breaking cases in shallow water, including marginal breaking events, to confirm the validity of the breaking inception threshold value $B_{th} \approx 0.85$ in a universal sense.

The transition from breaking to non-breaking of shoaling waves over a plane beach may only occur close to the shoreline, where an accurate estimation of B is challenging, as discussed above. Thus we consider the behaviour of B for regular, irregular, and solitary waves, as well as focused packets, propagating over a submerged bar (Figure 1b), with an emphasis on marginally breaking cases. In the following, we present and discuss the computed temporal variation of B for cases of simulated regular and solitary waves. Cases with irregular waves and focused wave packets will be reported elsewhere.

Figure 6 shows the temporal evolution of two evolving crests and their corresponding B values for non-breaking and breaking regular waves ($T_w = 1.01$ s) propagating over a submerged bar, as defined in Figure 1b. Each row shows LES/VOF results for a case with an initial wave height H_w , where increasing H_w results in a transition from non-breaking (Frames a-d) to intermittent breaking (Frames e and f) and breaking (Frames g-j) events. For each individual evolving crest, the reference time is the time at which B transitions through 0.85 or

426 reaches its maximum for breaking and non-breaking cases, respectively. Although incident
427 crests with the same H_w have exactly the same initial wave conditions, their kinematics and
428 dynamics near the break point or crest maximum are not the same, due to their interaction
429 with the low-frequency waves in the numerical tank (e.g., seiches), the residual motions due
430 to preceding waves, etc. Although these variations have a relatively small effect on the height
431 of the evolving crests, they may result in an intermittent breaking, as shown in Frames (e)
432 and (f).

433 Figure 7 shows similar results as in Figure 6 but for the solitary wave cases, computed
434 using the BEM model. Results shown in Figure 6 and Figure 7 confirm the validity of $B_{th} \approx$
435 0.85 as a robust predictor of breaking onset in shallow water.

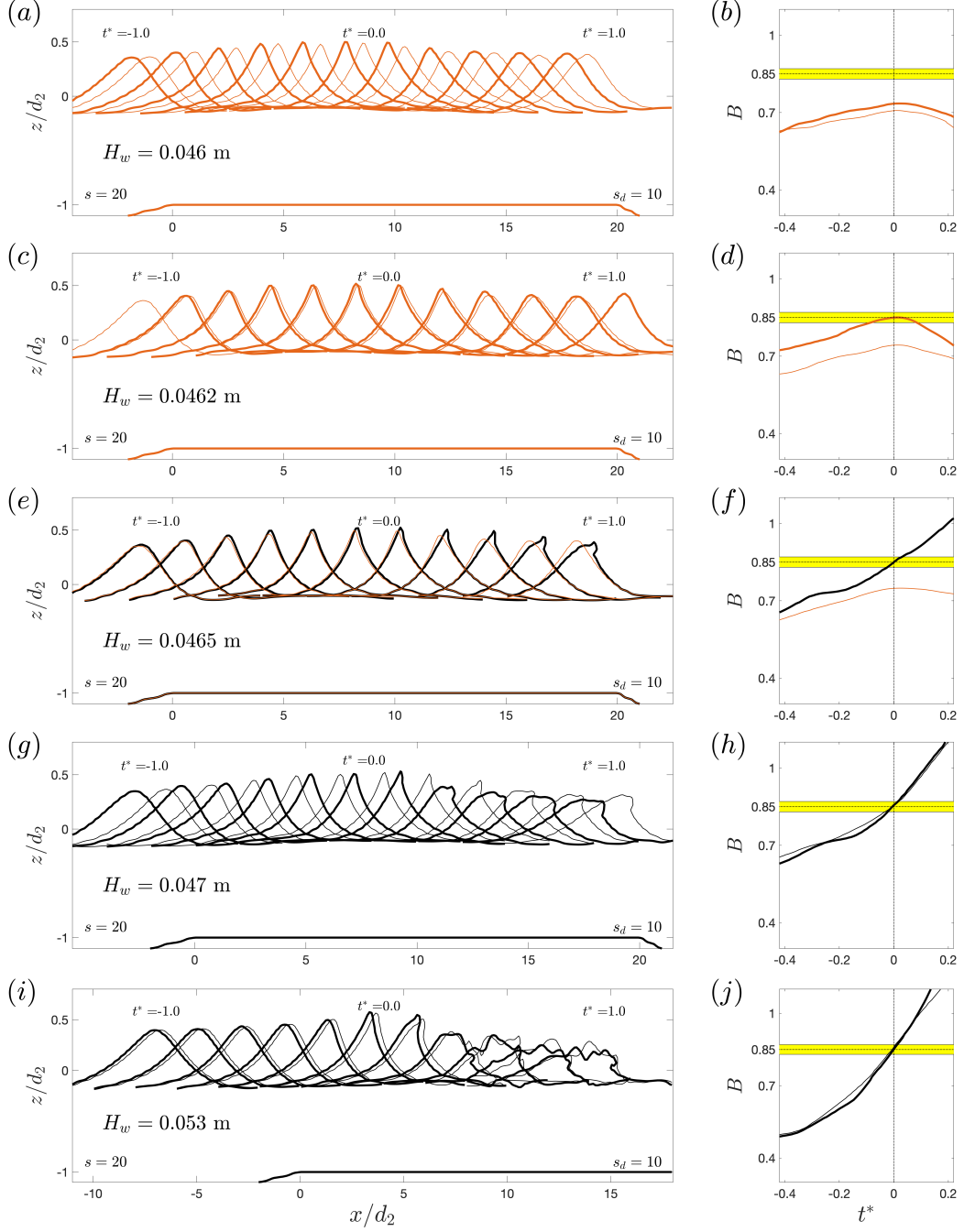


Figure 6: Temporal evolution of (a, c, e, g, i): wave profiles and (b, d, f, h): the breaking onset parameter B for two different evolving crests of a regular wave ($T_w = 1.01$ s) propagating over a bar with a front slope $m = 1/s$, demonstrating a transition from non-breaking to spilling breaking with an increasing ξ_0 . Here d_2 is the still water depth over the top of the bar (Figure 1b). All results are obtained using the LES/VOF model. The yellow regions indicate $B = 0.85 \pm 0.02$.

436 **4.3 Summary of the results**

437 Figure 8 shows the variation of the maximum B values as a function of the wave Froude
 438 number F (defined in §5.1 below) for all simulated crests, using LES/VOF and BEM models,
 439 from deep to shallow water. As mentioned above, we observe that if B transitions through
 440 the threshold value $B_{th} \approx 0.85$ it will attain the level $B = 1$ when the surface signatures of
 441 breaking appear for all cases. The two exceptional breaking wave cases indicated by + signs
 442 below $B = 1$ represent solitary wave cases simulated using the BEM model, where the sim-
 443 ultations stop before breaking onset due to insufficient spatial resolution. We observe that the
 444 breaking inception threshold values B_{th} , beyond which the crest evolves to breaking, range
 445 between 0.85 and 0.88 in shallow water wave breaking. This is consistent with the relevant
 446 previous studies of the variation of B_{th} in intermediate depth and deep water [Barthelemy
 447 *et al.*, 2018; Saket *et al.*, 2017, 2018; Derakhti *et al.*, 2018]. The plot also displays a dotted
 448 line corresponding to the linearized relation $B = F$. We observe that the maximum occurring
 449 values of B for all the tabulated steep but nonbreaking crests greatly exceed this lower limit,
 450 due to a combination of underprediction of fluid velocity in the crest as well as possible re-
 451 ductions of crest speed prior to breaking in intermediate depth cases.

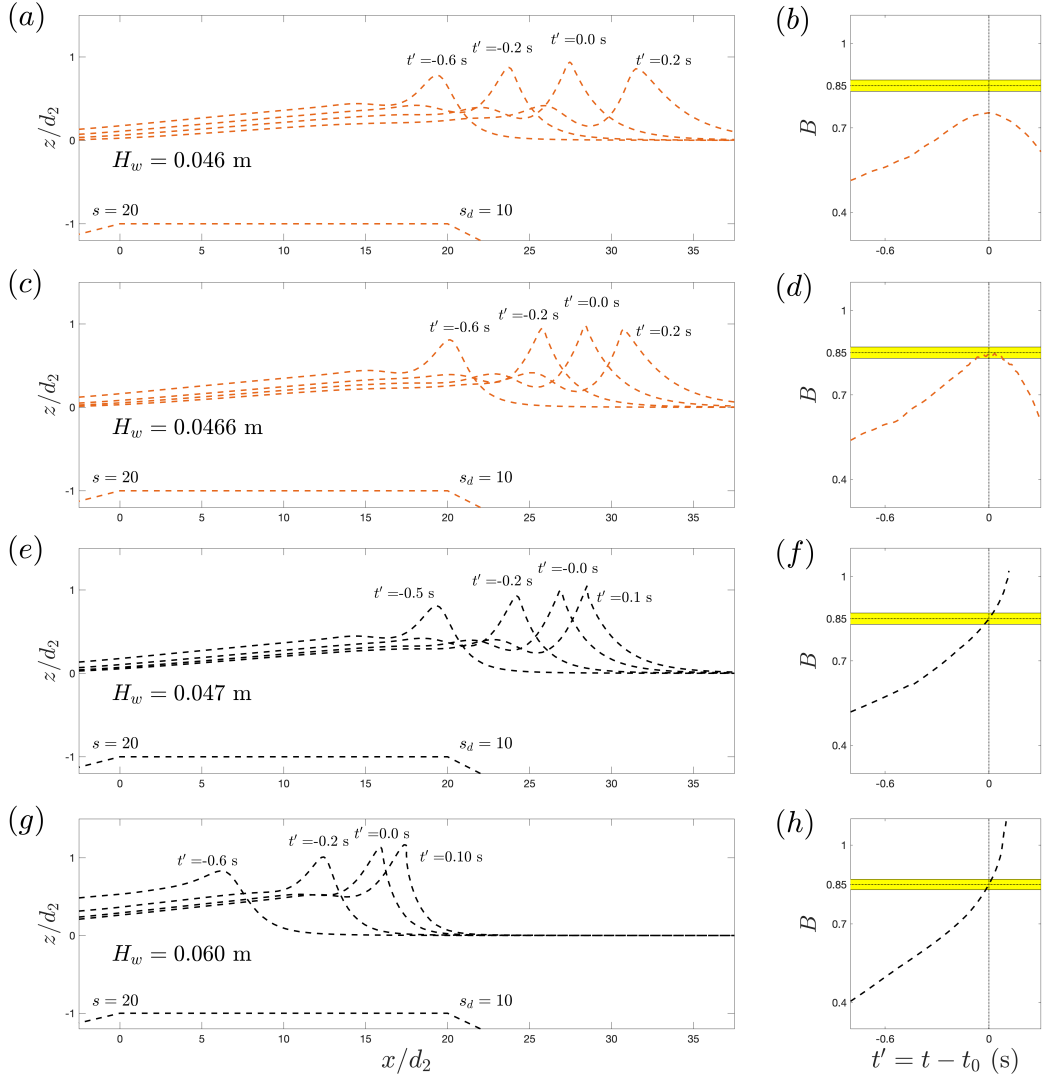


Figure 7: (a, c, e, g): Snapshots of the free surface elevations and (b, d, f, h): temporal evolution of the breaking onset parameter B , for solitary waves propagating over a bar with a front slope $m = 1/s$ demonstrating a transition from non-breaking to spilling breaking with an increasing initial wave height. Here d_2 is the still water depth over the top of the bar (Figure 1b). All results are obtained using the BEM model. The yellow regions indicate $B = 0.85 \pm 0.02$.

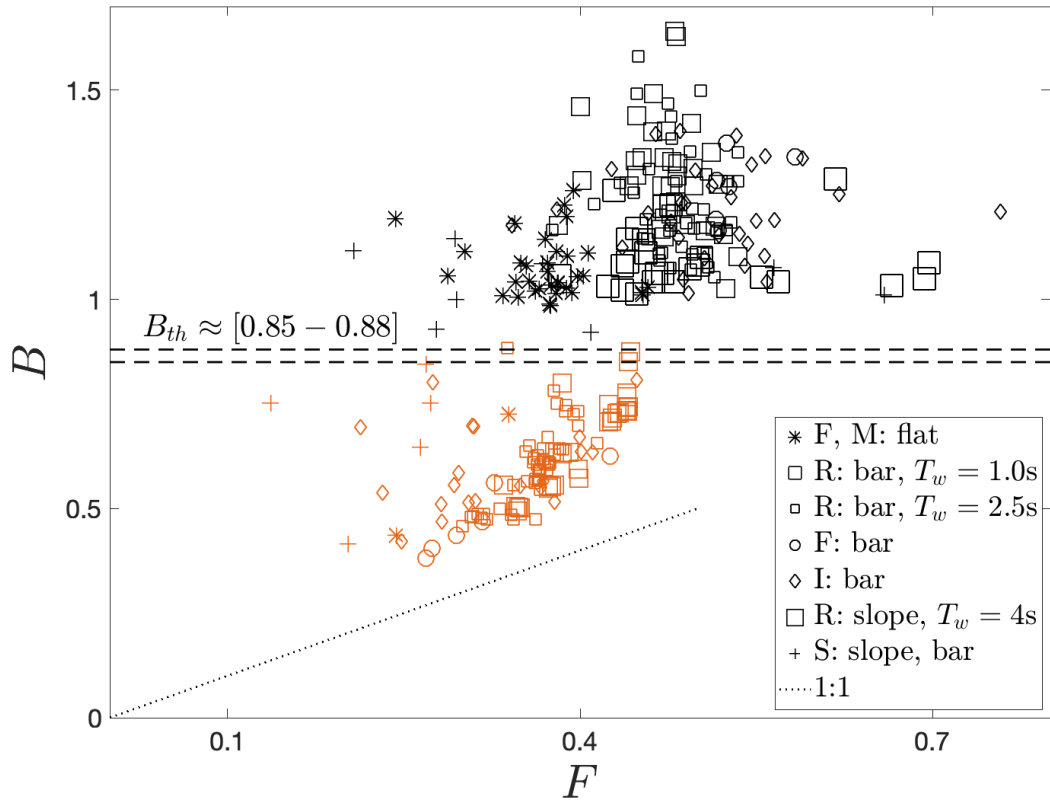


Figure 8: Maximum value of the breaking onset parameter B as a function of the wave Froude number F , for all breaking (black symbols) and non-breaking (orange symbols) wave crests. In the breaking cases, the maximum value of B corresponds to the time, after the onset of breaking, at which the location of the crest maximum becomes noisy.

452 **5 Discussion**

453 In this section, we present an evaluation of the other existing breaking criteria from the
 454 literature. These are the various geometric parameters defined below, which are applied to
 455 the simulated wave trains. Next, we comment on the extension of the results to 3D shoaling
 456 and breaking waves in shallow water. Finally, we discuss the implementation of the parameter
 457 B in energy-conserving phase-resolving models.

458 **5.1 Definition of local geometric parameters used in the analysis**

459 Following *Beji* [1995], we define a wave Froude number

$$460 \quad F = gH/2c_{lin}^2, \quad (14)$$

461 where $c_{lin}^2 = gk^{-1} \tanh kd$ and $k = 2\pi/L$ is the local wave number. We note that F simplifies to the nonlinearity parameter $\gamma/2$ in shallow water and to the local steepness $S = kH/2$ in deep water. Thus, F may be considered to be a unified nonlinearity parameter in arbitrary depth [*Beji*, 1995; *Kirby*, 1998]. Further, using the results from linear theory, we can readily obtain $F = u_{lin}/c_{lin} = B_{lin}$, where u_{lin} is the linear theory prediction of the particle velocity at the horizontal crest position and at the mean water level. All of these properties suggest that F is a preferable diagnostic geometric parameter compared to γ and S for a unified breaking onset criterion in arbitrary depth.

468 We define a wave front slope θ in degrees by

$$469 \quad \theta = \frac{180}{\pi} \tan^{-1}(H_c/l_1), \quad (15)$$

470 where H_c/l_1 is the crest front steepness (see Figure A.1). We further define $\mathcal{A}_v = H_c/H$
 471 and $\mathcal{A}_h = l_1/l_2 - 1$, which represent instantaneous vertical and horizontal asymmetry of
 472 the evolving crest, and are related to the statistical third-order moments, normalized wave
 473 skewness $\overline{\eta^3}/\overline{\eta^2}^{3/2}$ and asymmetry $\overline{\mathcal{H}(\eta)^3}/\overline{\eta^2}^{3/2}$ (where \mathcal{H} denotes the Hilbert transform),
 474 respectively. Finally, we define $\mathcal{A}'_h = l'_1/l'_2 - 1$, which represents the horizontal asymmetry of
 475 the shape of the crest but only considering the upper half part of the crest. \mathcal{A}'_h is also applicable
 476 for crests without zero-crossing points and is a more robust measure compared to \mathcal{A}_h for crests with noticeable irregularity at their back face (Figure A.2b).

477 The parameter θ is often used as the diagnostic criterion for the onset of breaking in
 478 Boussinesq models using eddy viscosity-type dissipation to model breaking [see, for example,
 479 *Schäffer et al.*, 1993; *Kennedy et al.*, 2000]. A maximum value of θ has also been used

480 as a breaking criterion in potential flow models. Thus, in their 2D-FNPF-BEM model, *Guig-*
 481 *nard et al.* [2001] used a maximum slope criterion to trigger dissipation using an “absorbing
 482 surface pressure”. *Grilli et al.* [2019] revised and extended this earlier work and *Papoutsel-*
 483 *lis et al.* [2019] implemented and tested a similar criterion and energy absorption method in
 484 their 2D-FNPF model. Finally, *Mivehchi* [2018] used a combination of maximum front slope
 485 and crest curvature as a breaking criterion in his 3D-BEM model. Note that in such energy
 486 conserving models, the energy of breaking waves is dissipated by applying an “absorbing”
 487 surface pressure specified opposite and proportional to the free surface velocity or similar.

488 5.2 Evaluation of predictive skills of existing geometric breaking criteria

489 Figure 9 shows examples of computed temporal variation of the various geometric
 490 parameters defined in §5.1 (also in Figure A.1) for breaking (black lines and symbols) and
 491 non-breaking (orange lines and symbols) wave crests from shallow to deep water. Examples
 492 shown in frames (a-f) represent regular waves shoaling over a submerged bar with a front
 493 face slope of 1/20 (Figure 1b), in which breaking is typically observed over the flat region of
 494 the bar and is characterized as shallow breaking. Examples shown in frames (g-l) represent
 495 focused packets and modulated waves propagating in intermediate and deep water over con-
 496 stant depth. Further, Figure 10 shows variation of the four geometric parameters γ , S , F and
 497 θ (§ 5.1) at the time when $B = 0.85$ or at the unbroken crest maximum, for which $t^* = 0$, for
 498 all simulated breaking (black symbols) and non-breaking (orange symbols) wave crests from
 499 shallow to deep water (which includes cases shown in Figure 9).

500 The most commonly used breaking onset parameter in shallow water wave breaking
 501 is $\gamma = H/d$; in phase-averaged models the mean depth $d + \bar{\eta}$ is typically used instead of
 502 still water depth d , such that mean wave set-up or set-down is included. There is a large body
 503 of literature including laboratory and field studies attempting to define γ values at breaking
 504 onset for various incident waves in shallow water. An extensive review is given in *Robert-*
 505 *son et al.* [2013]. Observed values of γ at breaking onset, in a wave-by-wave sense, are typ-
 506 ically greater than 0.6 in shallow water. Consistent with the existing relevant literature, re-
 507 sults shown in Figures 9a and 9g indicate that γ increases as a wave approaches the break-
 508 point and that γ at breaking onset is an increasing function of the surf-similarity parameter
 509 ξ_0 [Battjes, 1974; Raubenheimer et al., 1996]. However, no unified formulation of γ predict-
 510 ing the onset of depth-limited wave breaking can be found (see Figure 10a). Further, it is

511 clear that γ is an irrelevant parameter for estimating the breaking onset of steepness-limited
 512 wave breaking in deep water.

513 In the shallow breaking cases shown in Figure 9a, the local depth d decreases over the
 514 front face of the bar (the shoaling region), then becomes constant over the top of the bar, and
 515 then increases over the back face of the bar (Figure 1b). The latter explains the noticeable
 516 decrease of γ for $t^* > 0$ for non-breaking crests. During the time a non-breaking crest propa-
 517 gates over the top of the bar (constant depth region) the variation of γ is relatively small.

518 Figures 9b and 9h indicate that as a crest approaches breaking, or its maximum height
 519 for non-breaking crests, the local steepness $S = kH/2$ increases both in shallow and deep wa-
 520 ter cases. We observe that the maximum steepness values of all the simulated non-breaking
 521 crests are smaller than that given by the *Miche* [1944] breaking steepness criterion $S =$
 522 $\pi/7 \tanh kd$ (dashed line in Figure 10b). We also observe that a large number of simulated
 523 breaking crests occur with a steepness value smaller than the limiting criterion. We note that
 524 our definition of L is different from the classical definition for wavelength; our L is much
 525 smaller than the latter in some of the shallow breaking cases considered here (see Appendix
 526 A). In summary, breaking is clearly related to steepness, but a unified formulation that is able
 527 to predict maximum values of S at breaking onset from deep to shallow water remains un-
 528 known; the same conclusion holds for the wave Froude number F (Eq. 14) (Figure 10c).

529 Figures 9c and 9i as well as Figure 10d document the variation of the wave front slope
 530 θ (Eq. 15) as a function of time and at $t^* = 0$, respectively, from shallow to deep water. In
 531 general, breaking crests have higher maximum values of θ compared to non-breaking crests.
 532 However, most of the spilling breakers, both in deep and shallow water, maintain their max-
 533 imum θ values as they approach the breakpoint. Moreover, θ decreases slightly as a crest
 534 approaches breaking in marginal breaking cases, both in deep and shallow water. These ob-
 535 servations suggest that θ might be a useful diagnostic breaking onset parameter but should
 536 be combined with other parameters; such as γ in shallow and with S (shown in Figure 10e)
 537 in deep water or, more generally, with the wave Froude number F (shown in Figure 10f) in
 538 order to potentially predict the breaking onset time and location in a phase resolved sense.

539 Finally, frames (d) - (f) and (j) - (l) of Figure 9 demonstrate that neither the horizontal
 540 (\mathcal{A}_h and \mathcal{A}'_h) nor the vertical asymmetry of an evolving crest (as defined in § 5.1) are a good
 541 candidate as a breaking onset parameter. Further, results show that some of the simulated
 542 wave crests, both in shallow and deep water, are remarkably symmetric just prior to breaking

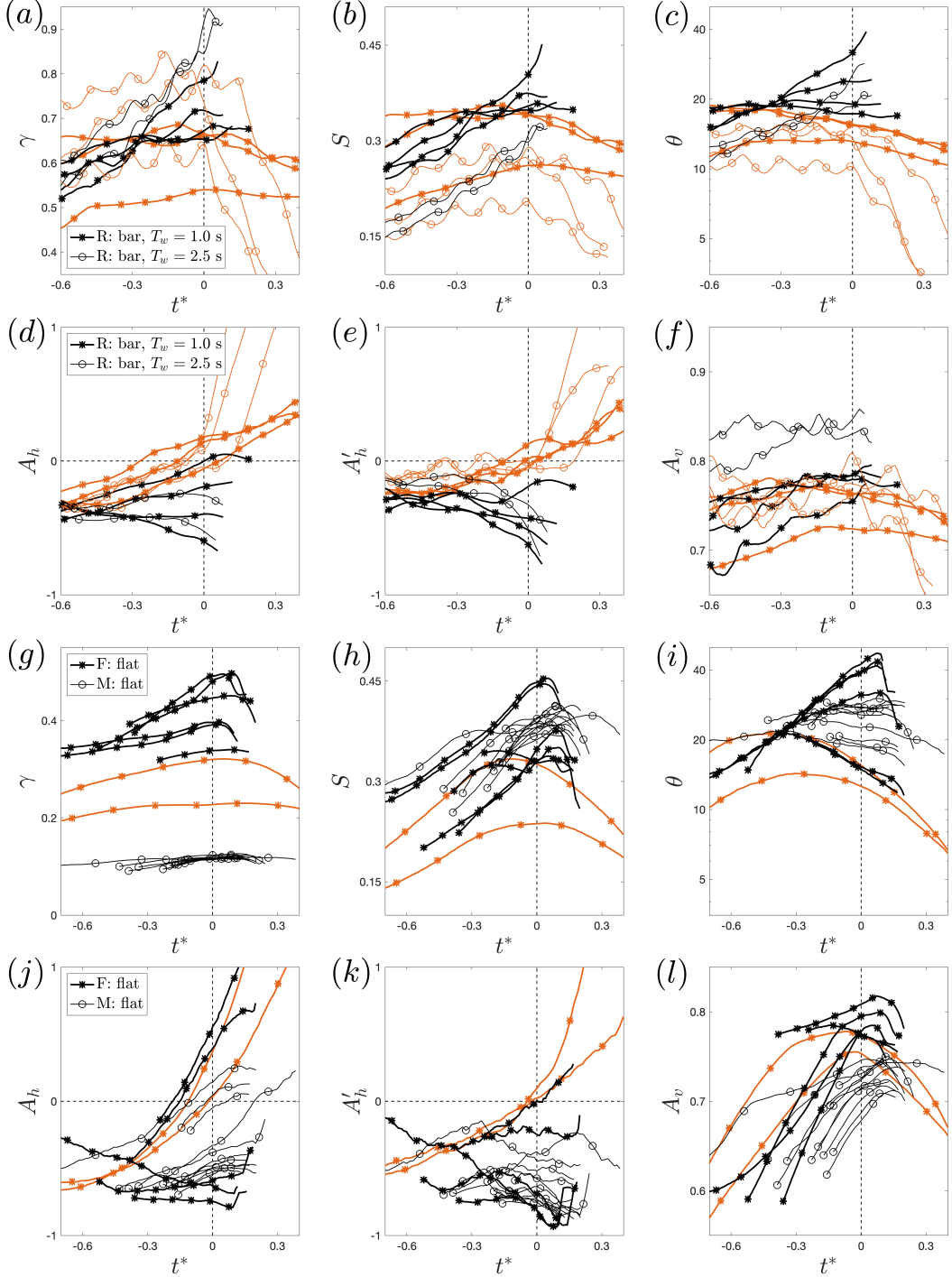


Figure 9: Examples of temporal evolution of various geometric parameters defined in §5.1 (also see Figure A.1) for breaking (black lines and symbols) and non-breaking (orange lines and symbols) wave crests (a – f): in shallow water, and (g – l): in intermediate depth and deep water. The capital letters in the legend indicate the type of incident waves, R: regular waves, F: focused packets, and M: modulated wave trains. In the legend, bar and flat denote bar geometry (Figure 1b) and flat bed (Figure 1c) respectively, and T_w is the period of the regular incident waves.

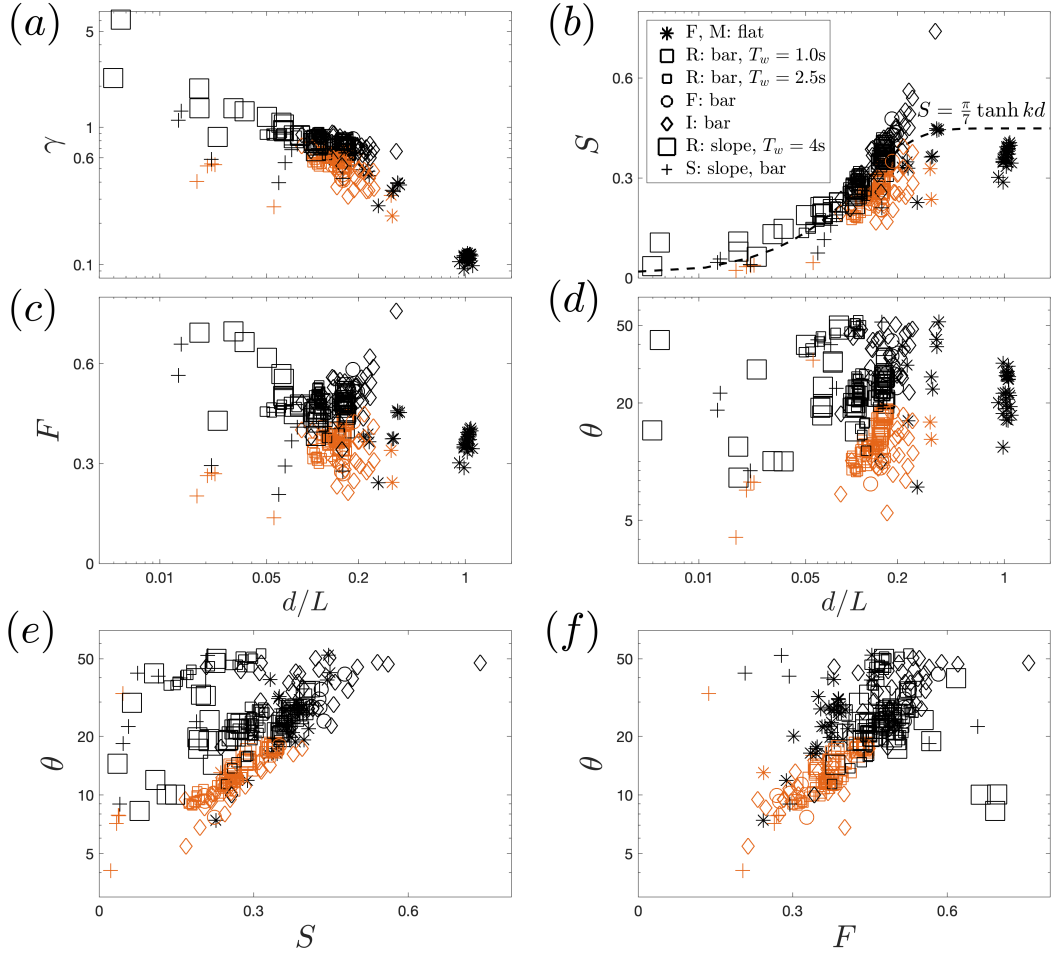


Figure 10: Variation of various geometric parameters, defined in §5.1, at the breaking inception time or crest maximum, for all simulated breaking (black symbols) and non-breaking (orange symbols) wave crests from deep to shallow water. The capital letters in the legend refer to the type of incident waves, R: regular, I: irregular, S: solitary waves, F: focused packets, and M: modulated wave trains. Here, $\gamma = H/d$ is the nonlinear parameter (or breaking index), $S = \pi H/L$ is the wave steepness, $\theta = 180/\pi \tan^{-1}(S^f)$ is the wave front slope (all are defined in Figure A.1), and $F = ga/c_{lin}^2$ is the wave Froude number.

543 ($\mathcal{A}_h \approx 0$). This result is consistent with field observations made using stereo photography in
 544 deep water [Schwendeman and Thomson, 2017] and with field observations using LIDAR in
 545 shallow water [Carini, 2018].

546 In summary, our results reveal that a criterion using both θ and F has relatively higher
 547 skill in predicting the onset of breaking from deep to shallow water, compared to the other
 548 geometric parameters considered here. However, such a criterion still cannot segregate all
 549 breaking crests from non-breaking ones.

550 **5.3 Two- versus three-dimensional shoaling and breaking waves**

551 While, in shallow water, most breakers end up being locally nearly 2D, 3D processes
 552 of directional and bathymetric focusing can affect or even govern the evolution of shoaling
 553 waves towards breaking. Earlier work with 2D- and 3D-BEM models, however, indicates that
 554 whether in 2D [Grilli *et al.*, 1997] or 3D [Guyenne and Grilli, 2006] once a wave approaches
 555 breaking onset, there is a “loss of memory” of the physical phenomenon(a) that have led
 556 to breaking and whether a crest breaks or not and how it breaks essentially depends on lo-
 557 cal wave properties (here represented by U and C at the crest). Guyenne and Grilli [2006],
 558 for instance, compared properties of solitary waves shoaling over a 3D sloping ridge or a
 559 2D plane slope in their 3D-BEM model and found similar velocity and acceleration fields
 560 near the crest and in the jet of breaking waves. This supports the present investigation of 2D
 561 shoaling and breaking waves in shallow water. Nevertheless in future work, we will consider
 562 more complex shallow water bathymetries and confirm the validity of the breaking inception
 563 threshold value $B_{th} \approx 0.85$ for breaking wave crests in such more realistic 3D shoaling cases.

564 **5.4 Implementation of the parameter B in energy-conserving phase-resolving 565 models**

566 The new criterion is suitable for use in wave-resolving models that cannot intrinsi-
 567 cally detect the onset of wave breaking. Some of these models, such as High Order Spec-
 568 tral (HOS) models [Dommermuth and Yue, 1987; West *et al.*, 1987], become unstable if they
 569 reach the visible breaking onset stage, *i.e.*, $B = 1$. Thus, warning of imminent breaking onset
 570 at $B_{th} \approx 0.85$ is critical in the context of the successful application of the new criterion in
 571 such wave-resolving energy-conserving models; because at $B = B_{th}$ the waveform is well de-
 572 fined, no vertical tangent occurs on the wave front face, and the free surface is single-valued.

573 In a practical implementation of the B_{th} criterion in wave models such as HOS or
 574 Boussinesq, one would be able to track the evolution of $B = U/C$ up to the point where the
 575 criterion is verified, provided wave crests can be identified. This was already demonstrated
 576 for simple 2D shoaling solitary waves, for instance, by *Wei et al.* [1995] using a fully nonlin-
 577 ear Boussinesq model and by *Seiffert and Ducrozet* [2018] for HOS. While a crest location
 578 and its velocity C can be easily computed in these 2D models, this is more difficult to do in
 579 3D. *Stansell and MacFarlane* [2002] identified crests in experimental results and computed
 580 their velocity c based on a Hilbert transform of the free surface. This method was applied
 581 by *Mivehchi* [2018] to detect wave crests and compute their velocity in results of a 3D-BEM
 582 model, and suppress breaking waves by specifying an “absorbing surface pressure”; here
 583 breaking was based on a maximum crest curvature/front-slope criterion. A similar Hilbert-
 584 transform-based method could be applied to detect crests and compute their celerity in re-
 585 sults of (2D horizontal) HOS or Boussinesq models. In the Boussinesq model, the particle
 586 velocity at the crest would be obtained from extrapolating to the surface the horizontal veloc-
 587 ity used in the model at some pre-defined depth, using the model’s assumed velocity profile
 588 (e.g., parabolic). This could be facilitated by formulating the Boussinesq model with a verti-
 589 cal boundary-fitted σ coordinate (as recently proposed by *Kirby* [2020]), which enables the
 590 simple projection of the model horizontal velocity to $\sigma = 1$.

591 6 Conclusions

592 The model simulation results presented here extend the results of B18 to cases of waves
 593 shoaling and breaking in shallow water. The local energy flux parameter B exceeding the
 594 threshold of ≈ 0.85 is confirmed to provide a robust predictor of breaking onset for cases
 595 where breaking results from a crest instability. In particular, we have simulated cases where
 596 a weak modulation of periodic waves by tank seiching leads to occasional breaking events in
 597 a train of otherwise unbroken waves, which are marginally close to breaking. These break-
 598 ing events are clearly indicated by the passage of B through the ≈ 0.85 threshold. Further, we
 599 have shown that $B_{th} \approx 0.85$ clearly separates breaking and non-breaking cases for shoaling/de-
 600 shoaling waves propagating over bars. We conclude that this investigation provides further
 601 support for the generic applicability of the new breaking framework proposed by B18, which
 602 was developed with specific reference to the onset of instability and incipient overturning in
 603 the region localized around wave crests.

604 Our extension to shoaling waves introduces the additional phenomenon of surging
 605 breakers, with breakdown and generation of turbulence during the uprush of a surging wave
 606 on a beach. This may be related more directly to instabilities of the strongly curved flow
 607 closer to the toe of the surging wave front. This process is very different in nature from the
 608 mechanism covered by the analysis of B18 and occurs without a crest-based criterion being
 609 exceeded. It thus represents a different route to breaking whose occurrence (or onset) would
 610 require an alternate criterion to be developed.

611 We emphasize that the validity of the proposed criterion also needs to be examined
 612 in the presence of wind forcing. The laboratory work of *Saket et al.* [2018] showed that
 613 $B_{th} \approx 0.85$ also segregates breaking from non-breaking crests in the presence of wind forcing
 614 in deep water breaking. A number of high-fidelity two-phase flow simulations of breaking
 615 waves in the presence of wind forcing [e.g., *Tang et al.*, 2017; *Yang et al.*, 2018] have
 616 been recently performed. Detailed quantification of the effect of direct wind forcing on the
 617 proposed breaking onset criterion in shallow water is left for future study.

618 **Acknowledgements:** This work was supported by NSF Physical Oceanography grants OCE-
 619 1756040 and OCE-1756355 to the Universities of Washington and Delaware. Computational
 620 support was provided by UD Instructional Technologies. MLB also gratefully acknowledges
 621 the support of the Australian Research Council for his breaking waves research through ARC
 622 DP120101701. SG gratefully acknowledge support from grant N00014-16-1270 from the
 623 US Office of Naval Research. The simulation data used in this paper can be accessed at UW
 624 Libraries Research Works, <https://digital.lib.washington.edu/researchworks>, and used under
 625 Creative Commons Attribution 4.0 International Public License.

626 **A: Sensitivity of local geometric parameters used in the analysis**

627 Definitions of the various local geometric parameters for an evolving wave crest are
 628 described in Figure A.1. Among these, the height H and length L of the carrier wave need
 629 to be defined first. Two main sources of uncertainty in the value of the geometric parameters
 630 defined in § 5.1 are the selected definitions of the local length L and height H of an evolving
 631 crest. Here we quantify such uncertainties in detail. In summary, using definitions other than
 632 those used here may vary the estimated H values for extreme waves by up to 10%. However,
 633 the sensitivity of the estimated L values at breaking onset are noticeably larger, especially for
 634 shallow cases.

Following *Derakhti and Kirby* [2016], D18 and *Tian et al.* [2008], we define the local wave length $L = 2l_{zc}$, where $l_{zc} = l_1 + l_2$ (Figure A.1) is the distance between the two consecutive zero-crossing points adjacent to the crest. We note that the zero-crossing point on the back face of the wave may have noticeably large fluctuations due to the presence of higher harmonics in shallow water cases (Figure A.2b) or high-frequency components in random waves, etc. Further, in some shallow water cases, *e.g.*, solitary waves, there are no zero-crossing points and thus l_{zc} can not be defined.

To resolve these issues, we fit a skewed-Gaussian function to the instantaneous wave profile and then estimate a length scale l_{zc}^{sg} from the skewed-Gaussian fitting as described below (Figure A.2). Finally, we take $L = \text{Min}(2l_{zc}, 2l_{zc}^{sg})$ as the local wave length.

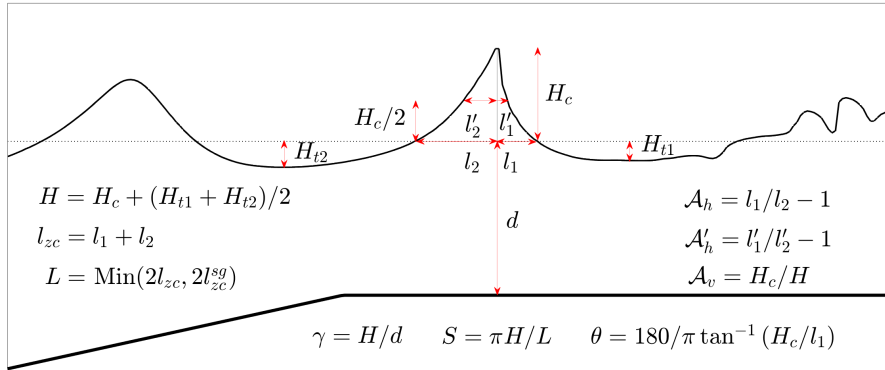


Figure A.1: Local geometric parameters describing an evolving wave crest. Here l_{zc}^{sg} represents a length scale obtained from a skewed-Gaussian fit to the crest region. Dotted and thick solid lines show the still water and the bed elevations respectively. The incident waves are propagating from left to right.

Here l_{zc}^{sg} is a length scale obtained from the skewed-Gaussian fit $f(r)$ defined as a scaled product of the standard normal probability density function $\phi(r) = \exp[-r^2/2]/\sqrt{2\pi}$ and its cumulative distribution function $\Phi(r) = (1 + \text{erf}[r/\sqrt{2}])/2$ (erf denotes the error function) given by

$$f(r) = c_1 \phi(r) \Phi(\alpha r) + c_2, \quad (\text{A.1})$$

where $r = (x - x_p)/\omega$ with x_p and ω are the peak location and scale respectively, α the horizontal skewness parameter ($\alpha < 0$ for waves pitch forward), c_1 a scaling parameter and

651 c_2 a vertical offset. The instantaneous f for each crest is obtained by a nonlinear fitting of
 652 Eq. A.1, including five coefficients, to the corresponding simulated wave profile.

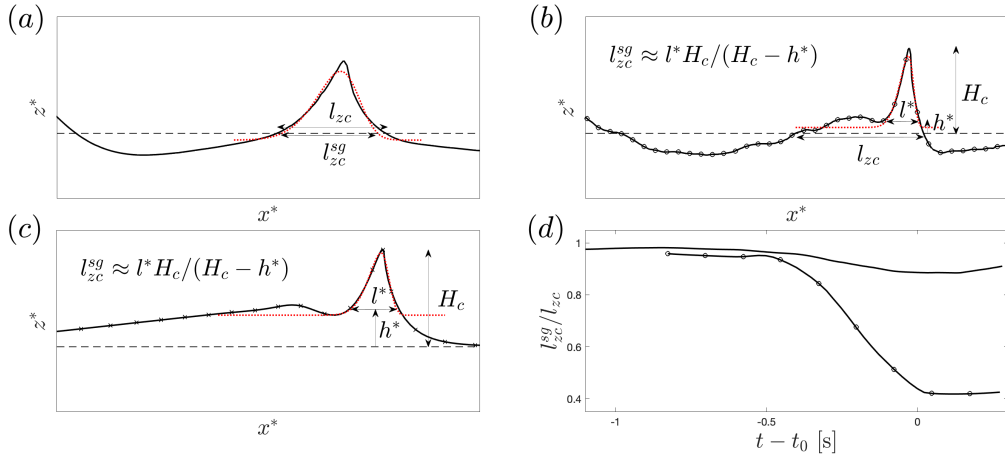


Figure A.2: (a, b, c) Definition of the local zero-crossing length-scale l_{zc}^{sg} obtained from skewed-Gaussian fitting (dotted lines) to the wave profile (solid lines) for examples of evolving crests shoaling over a submerged bar as well as (d) the temporal variation of l_{zc}^{sg}/l_{zc} before (shoaling phase) and after the breaking onset ($t = t_0$) for the crests shown in (a) and (b). (a) Regular waves with $T_w = 1.01$ s, (b) regular waves with $T_w = 2.525$ s, and (c) a solitary wave. Note that l_{zc} does not exist for solitary waves. In (a, b, c), the dashed lines show the still water levels.

653 Frames (a), (b), and (c) of Figure A.2 show examples of f (dotted lines) and the cor-
 654 responding l_{zc}^{sg} , just before breaking onset time, for three simulated evolving crests shoal-
 655 ing over a submerged bar. In addition, Figure A.2d shows the temporal variation of the ratio
 656 l_{zc}^{sg}/l_{zc} for the two examples shown in frames (a) and (b). Frames (b) and (d) show that we
 657 may have $l_{zc}^{sg} \ll l_{zc}$ at breaking onset in cases with irregularities on the back face of the
 658 wave, *e.g.*, due to the presence of higher harmonics. Finally, in solitary cases (Figure A.2c)
 659 we simply define $L = 2l_{zc}^{sg}$ because there are no zero-crossing points and thus l_{zc} cannot be
 660 defined.

661 At breaking onset, Figure A.3a demonstrates that the length scale l_{zc}^{sg} obtained from
 662 the skewed Gaussian fitting (Eq. A.1) is usually smaller than the zero-crossing length scale
 663 l_{zc} (Figure A.2). Our results show that $l_{zc}^{sg}/l_{zc} > 0.9$ in most cases, especially for those
 664 with $d/L_0 > 0.1$, with d the still water depth and L_0 a linear prediction of the local wave
 665 length obtained by using the linear dispersion relation $(2\pi/T_0)^2 = gk_0 \tanh [k_0 d]$ with d the

666 still water depth, $k_0 = 2\pi/L_0$ and T_0 equal to paddle period for monochromatic waves and
 667 peak period T_p for incident irregular waves. In some of the shallow cases ($d/L_0 < 0.1$),
 668 however, we observe l_{zc}^{sg}/l_{zc} values down to 0.4. Figure A.3b shows that our definition of
 669 L represents a smaller length scale compared to the characteristic wave length L_0 where the
 670 averaged values of L vary between $L_0/3$ in shallow water up to $0.7L_0$ in intermediate and
 671 deep water.

672 We define the local wave height H as the sum of a crest elevation and averaged trough
 673 elevations before and after the crest, $H = H_c + (H_{t1} + H_{t2})/2$. Our results (Figures A.3c and
 674 A.3d) indicate that other potential definitions of wave height such as $H_c + H_{t1}$ or $H_c + H_{t2}$ are
 675 within 10% of $H = H_c + (H_{t1} + H_{t2})/2$ in most cases from deep to shallow water. In addition,
 676 the downstream trough height H_{t1} is greater than or equal to the upstream trough height H_{t2}
 677 in shallow water cases; the trend is reversed in deep water cases. These trough heights vary
 678 between $0.2H_c$ and $0.5H_c$ in most cases.

679 B: Model validation for shallow water breaking

680 In this section, the validation of the LES/VOF model [Derakhti and Kirby, 2014a] in-
 681 cluding detailed comparisons of free surface evolution and organized and turbulent velocity
 682 fields, is presented for a number of available laboratory data for breaking and non-breaking
 683 waves in shallow water. The reader is referred to Derakhti and Kirby [2014a,b, 2016] for
 684 the detailed examination of the model prediction of the free surface evolution, organized
 685 and turbulent velocity fields, bubble void fraction, integral properties of the bubble plume,
 686 and the total energy dissipation compared with corresponding measured data, as well as the
 687 sensitivity of the simulation results with respect to the selected grid resolution for focusing
 688 laboratory-scale breaking packets in intermediate depth and deep water.

689 In all the simulated cases using the LES/VOF model, the selected horizontal grid size
 690 in the wave propagation direction (which is always $+x$ direction here) Δx is smaller than
 691 $1/100$ of the dominant wavelength at the x location at which the crest maximum was ob-
 692 served, and $\Delta z = \Delta y \leq \Delta x$. Using such spatial resolution, our LES/VOF model captures
 693 the free surface and organized velocity field fairly accurately up to the break point, and the
 694 estimates of the loss of total wave energy due to wave breaking are typically within 10% of
 695 observed levels [Derakhti *et al.*, 2018], after correcting for the change in the downstream
 696 group velocity following breaking in isolated breaking waves [Derakhti and Kirby, 2016].

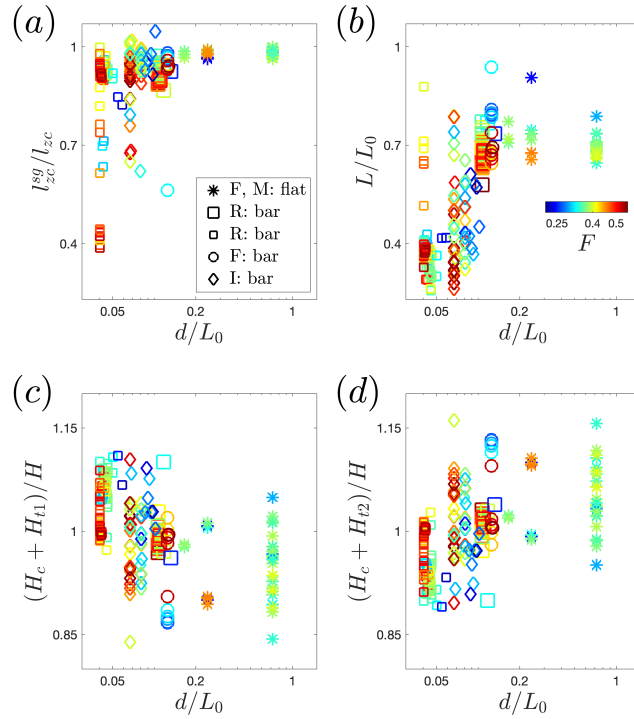


Figure A.3: Sensitivity of the local height and length of an evolving crest from deep to shallow water. (a) the ratio between the length scales l_{zc}^{sg} obtained from skewed-Gaussian fitting defined in Eq. (A.1) and l_{zc} both shown in Figure A.2; and (b) the ratio between the zero-crossing length scale $L = \text{Min}(2l_{zc}, 2l_{zc}^{sg})$ and a wave length L_0 at breaking onset for the breaking crests or at the time at which $H_c = \eta_{max}$ for the non-breaking crests. Here, L_0 is obtained by using the linear dispersion relation $(2\pi/T_0)^2 = g k_0 \tanh[k_0 d]$ with d the still water depth, $k_0 = 2\pi/L_0$ and T_0 equals to paddle period for monochromatic waves and peak period T_p for incident irregular waves.

Regarding the FNPF-BEM model used in this work, *Grilli et al.* [1994a] showed that surface elevations simulated with the model for solitary waves shoaling over plane slopes agreed within 1 – 2% with measured surface elevations, up to the breaking point. *Grilli et al.* [1994b] reported a similarly good agreement of numerical results with experiments for solitary waves propagating over a trapezoidal breakwater. *Grilli et al.* [1997] showed that the model could accurately predict breaking crest elevations, breaker index, and breaker types for solitary waves of various incident height propagating over mild to steep slopes. Finally, *Grilli et al.* [2019] show that the model also accurately simulates the shoaling and propagation of periodic waves over a bar similar to that considered here.

706 **B.1 Regular waves shoaling over a plane beach**

707 Here we consider the LES/VOF model performance for the case of regular depth-
 708 limited wave breaking on a planar beach (P10-r) in terms of phase-averaged free surface
 709 elevations and wave height using the data set of *Ting and Nelson* [2011]. We also compare
 710 the model results of the case P10-r with the free surface and velocity measurements of the
 711 spilling case of *Ting and Kirby* [1994]. The experimental set-up and incident wave condi-
 712 tions of the latter are similar as in P10-r and are also summarized in Table B.1. This experi-
 713 ment has been widely used by other researchers to validate both RANS [*Lin and Liu*, 1999;
 714 *Ma et al.*, 2011; *Derakhti et al.*, 2015, 2016a,b,c] and LES [*Christensen*, 2006; *Lakehal and*
 715 *Liovic*, 2011] numerical models.

716 Figure B.1 shows that the model captures the evolution of phase-averaged free sur-
 717 face elevations reasonably well compared with the corresponding measurements of *Ting and*
 718 *Nelson* [2011] in the shoaling, transition and inner surfzone. Further, Figure B.2 shows the
 719 comparison between the predicted and observed cross-shore variation of the wave height H
 720 calculated from the phase-averaged free surface time-series. Here phase averaging is per-
 721 formed over N successive waves after the wave field reaches a steady state condition, where
 722 N is 10 in both the simulated results and the measurements.

Case	H_w (mm)	T_w (s)	d_1 (m)	L_1 (m)	s	ξ_0	d_2 (m)	L_2 (m)	s_d	Exp.
P10-r	122	2.0	0.36	0	$\frac{100}{3}$	0.21	-	-	-	<i>Ting and Nelson</i> [2011]
	125	2.0	0.4	0	35	0.20	-	-	-	<i>Ting and Kirby</i> [1994]
B1-r	41.0	1.01	0.4	6	20	0.30	0.1	2	10	<i>Luth et al.</i> [1994]
B3-r	29.0	2.53	0.4	6	20	0.95	0.1	2	10	<i>Luth et al.</i> [1994]
B9-r	97.2	1.43	0.7	2	10	0.57	0.08	0	0	<i>Blenkinsopp and Chaplin</i> [2007]

Table B.1: Input parameters for the simulated cases used for the validation of the LES/VOF model. Definitions are given in table 1.

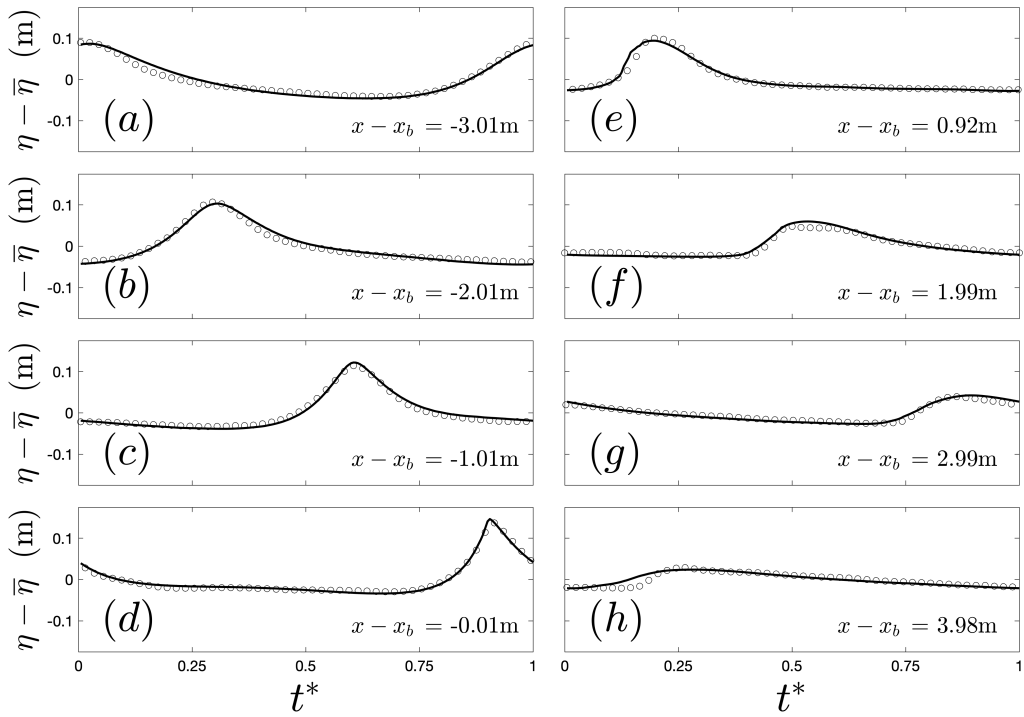


Figure B.1: Comparison between the LES/VOF model results of spanwise-phase-averaged free surface elevations at various cross-shore locations for the case P10-r and the corresponding measurements by *Ting and Nelson [2011]*. No spanwise averaging was involved in the measurement.

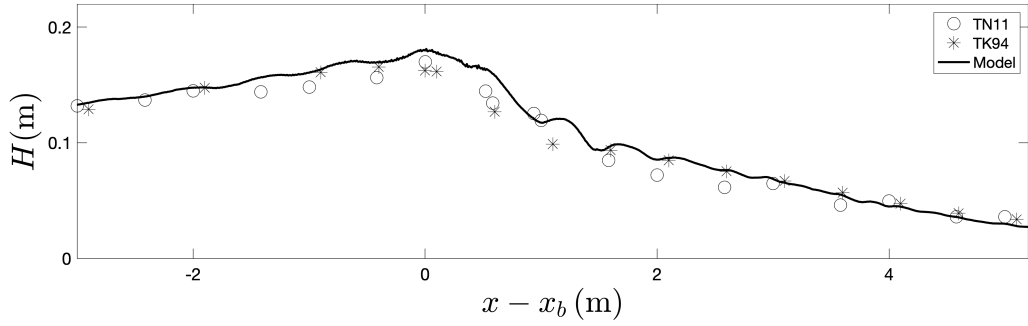


Figure B.2: The LES/VOF model-data comparison of the cross-shore variation of the wave height H for the case P10-r. Here TN11 and TK94 denote the data set of *Ting and Nelson* [2011] and *Ting and Kirby* [1994] respectively.

Figure B.2 also shows that the spatial evolution of H relative to the break point in the case P10-r is comparable with that in the spilling case of *Ting and Kirby* [1994]. Thus although the incident wave conditions and setup in the latter are slightly different than those in the case P10 the wave-driven currents and turbulence statistics should be comparable.

Figure B.3 shows the spatial distribution of the normalized spanwise-time-averaged, $\langle k \rangle^{1/2} / \sqrt{gh}$, turbulent kinetic energy for PS-a. Figure B.3 shows that both the magnitude and spatial variation of the predicted $\langle k \rangle^{1/2} / \sqrt{gh}$ and $\langle u \rangle / \sqrt{gh}$ are consistent with the corresponding measured values of *Ting and Kirby* [1994] in the transition and inner surf zone.

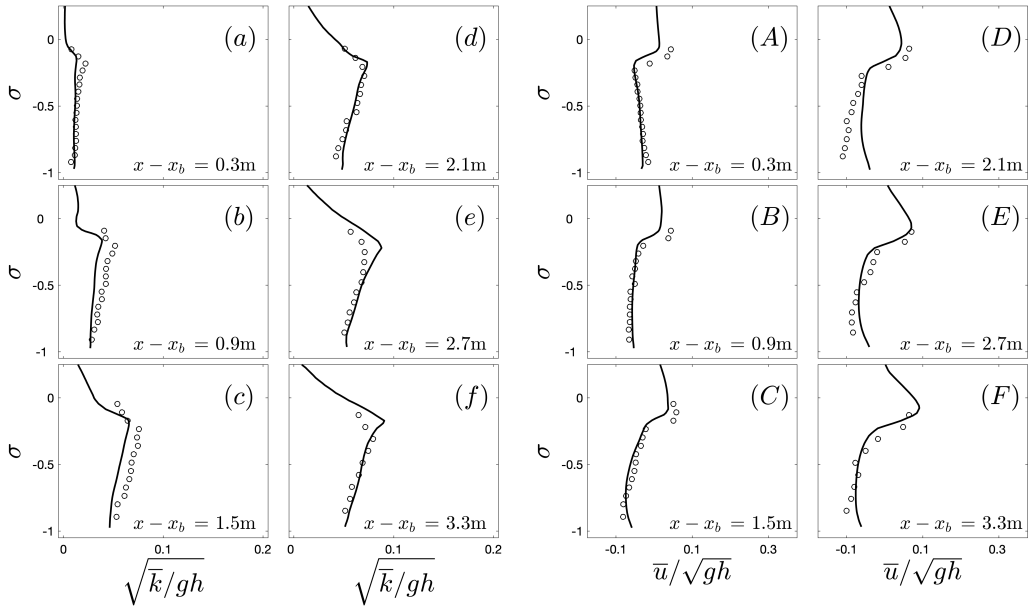


Figure B.3: The LES/VOF model results of spanwise-time-averaged normalized (a – f) turbulent kinetic energy, $\sqrt{k/gh}$, and (A – F) horizontal velocity, \bar{u}/\sqrt{gh} , (undertow) profiles for the case P10-r at various cross-shore locations after the initial break point. Circles show the measurements of *Ting and Kirby* [1994]. Here, $\sigma = (z - \bar{\eta})/h$ and $h = d + \bar{\eta}$.

731 **B.2 Regular waves shoaling over an idealized bar**

732 Here we consider the LES/VOF model performance for cases of regular non-breaking
 733 (B1-r) and breaking (B3-r and B9-r) waves shoaling over a submerged bar, using the data sets
 734 of *Luth et al.* [1994] and *Blenkinsopp and Chaplin* [2007]. Figures B.4 and B.5 documents
 735 that the model accurately captures the nonlinear evolution of evolving crests propagating over
 736 the up-slope ($-s(d_1 - d_2) < x < 0$) and top ($0 < x < L_2$) of the bar in all cases. Figure B.5
 737 also shows that the model fairly reasonably predicts the kinematics of the entrained bubble
 738 plume compared to the observations. The apparent mismatch between the predicted and ob-
 739 served wave profiles is mainly due to the mismatch between their corresponding incident
 740 waves and due to the difference between the low frequency wave climate in the numerical
 741 and laboratory wave tanks.

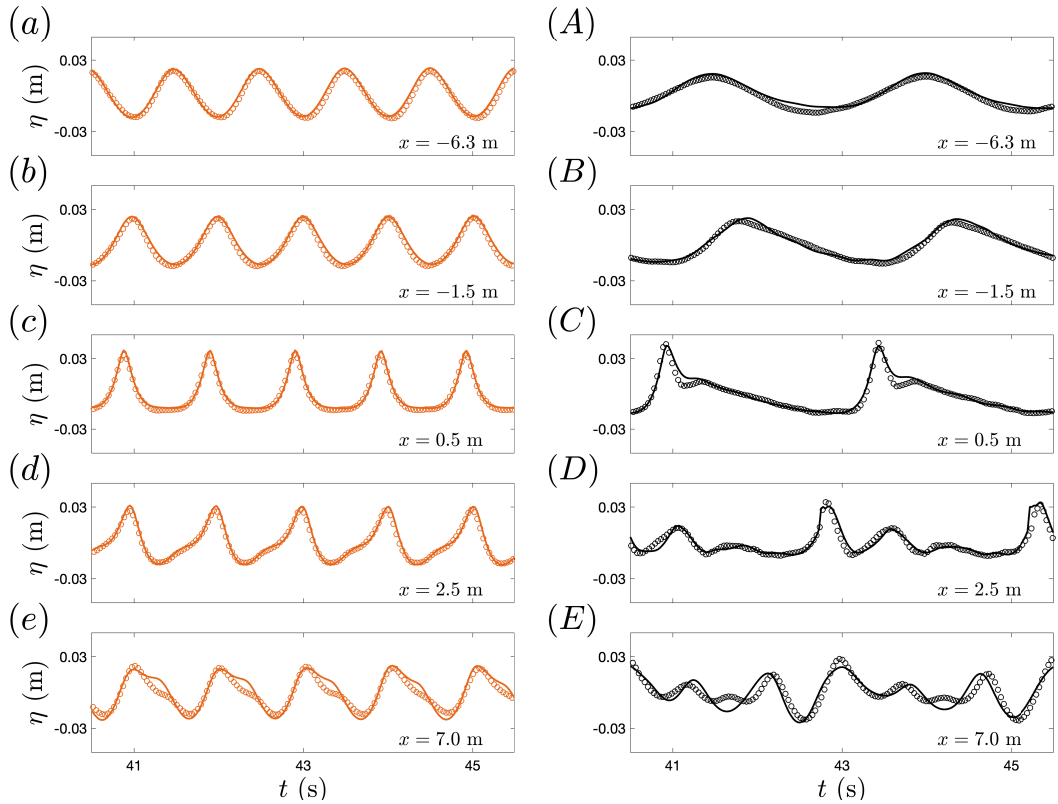


Figure B.4: Comparison of the LES/VOF model results (solid lines) and measurements [*Luth et al.*, 1994] (circles) of free surface elevations at various x locations for the along-crest uniform (a–e) non-breaking, with $T_w = 1.01$ s and $H_w = 0.041$ m, and (A–E) breaking, with $T_w = 2.525$ s and $H_w = 0.029$ m, regular waves shoaling over a submerged bar. Here $-6 < x < 0$ and $0 < x < 2$ indicate the up-slope and top of the bar respectively (see Figure 1c and Table B.1).

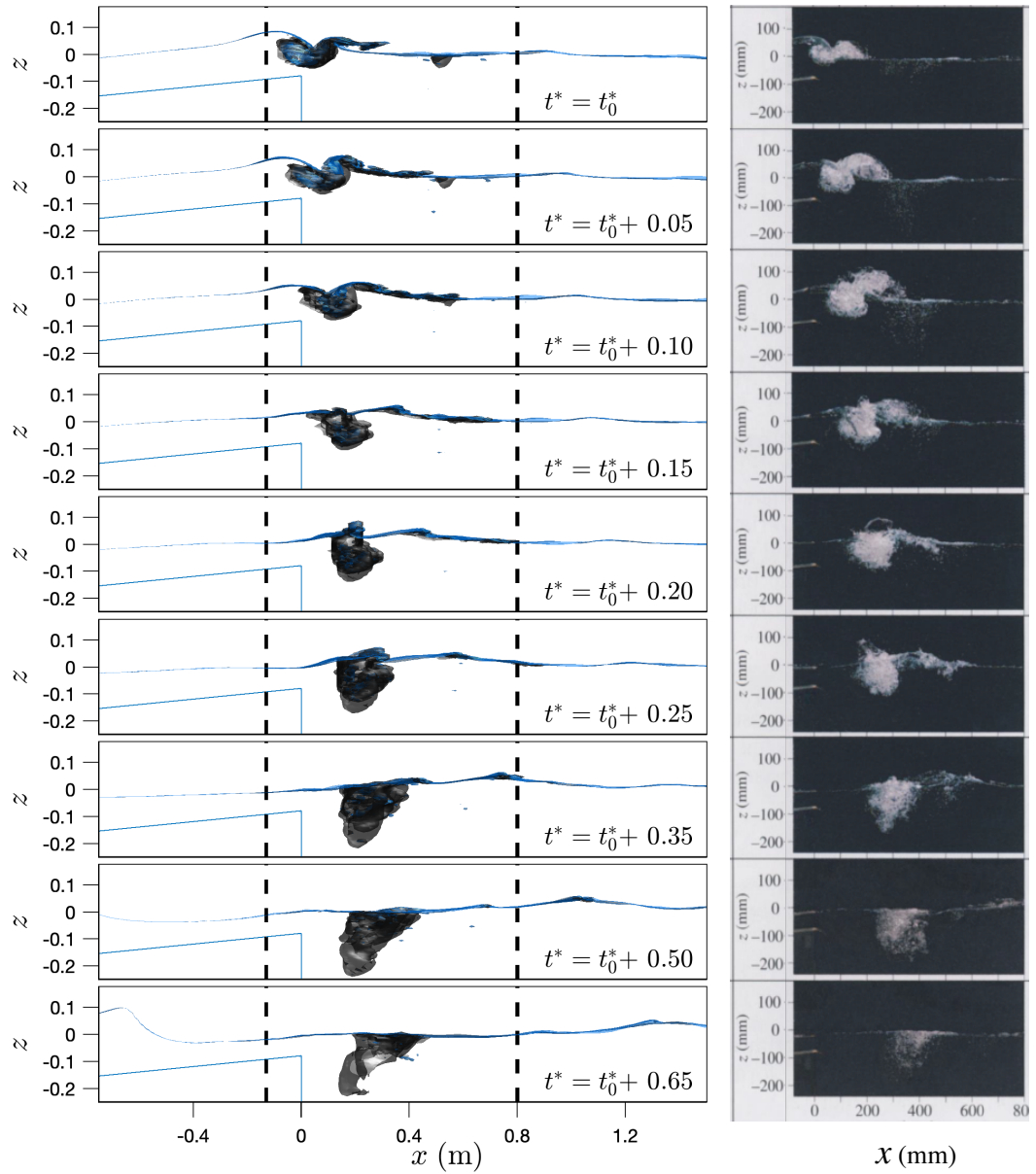


Figure B.5: Comparison of the side-view of the predicted (left column) and observed (right column) bubble plume evolution for the case B9-r. The two dashed lines in the right column indicate the field of view of the photographs, adopted from Blenkinsopp and Chaplin [2007, Figure 4].

742 **References**

743 Babanin, A., D. Chalikov, I. Young, and I. Savel'yev (2007), Predicting the breaking onset of
744 surface water waves, *Geophysical research letters*, 34(7), doi:10.1029/2006GL029135.

745 Banner, M., X. Barthelemy, F. Fedele, M. Allis, A. Benetazzo, F. Dias, and W. Peirson
746 (2014), Linking reduced breaking crest speeds to unsteady nonlinear water wave group
747 behavior, *Phys. rev. let.*, 112(11), 114,502, doi:10.1103/PhysRevLett.112.114502.

748 Banner, M. L., and W. L. Peirson (2007), Wave breaking onset and strength for two-
749 dimensional deep-water wave groups, *Journal of Fluid Mechanics*, 585, 93–115.

750 Banner, M. L., and D. H. Peregrine (1993), Wave breaking in deep water, *Annual Review*
751 *Fluid Mech.*, 25, 373–397.

752 Barthelemy, X., M. L. Banner, W. L. Peirson, F. Fedele, M. Allis, and F. Dias (2018), On a
753 unified breaking onset threshold for gravity waves in deep and intermediate depth water,
754 *Journal of Fluid Mechanics*, 841, 463–488.

755 Battjes, J. A. (1974), Surf similarity, in *Proceedings of the 14th International Conference on*
756 *Coastal Engineering*, pp. 466–480, ASCE.

757 Beji, S. (1995), Note on a nonlinearity parameter of surface waves, *Coastal Eng.*, 25, 81–85.

758 Blenkinsopp, C. E., and J. R. Chaplin (2007), Void fraction measurements in breaking waves,
759 *Proceedings of the Royal Society A*, 463, 3151–3170, doi:10.1098/rspa.2007.1901.

760 Booij, N. (1981), Gravity waves on water with non-uniform depth and current, Ph.D. thesis,
761 Technische Hogeschool, Delft (Netherlands).

762 Carini, R. J. (2018), Geometry, kinematics and energetics of surf zone waves near the onset
763 of breaking using remote sensing, Ph.D. thesis, University of Washington, Seattle, WA.

764 Carrica, P. M., D. Drew, F. Bonetto, and R. T. Lahey (1999), A polydisperse model for bub-
765 bly two-phase flow around a surface ship, *Int. J Multiphase Flow*, 25, 257–305.

766 Christensen, E. D. (2006), Large eddy simulation of spilling and plunging breakers, *Coastal*
767 *Engineering*, 53, 463–485, doi:10.1016/j.coastaleng.2005.11.001.

768 Craciunescu, C. C., and M. Christou (2019), Identifying breaking waves from measured time
769 traces, in *The 29th International Ocean and Polar Engineering Conference*, International
770 Society of Offshore and Polar Engineers.

771 Derakhti, M., and J. T. Kirby (2014a), Bubble entrainment and liquid bubble interaction un-
772 der unsteady breaking waves, *J. Fluid Mech.*, 761, 464–506, doi:10.1017/jfm.2014.637.

773 Derakhti, M., and J. T. Kirby (2014b), Bubble entrainment and liquid bubble interaction un-
774 der unsteady breaking waves, *Research Report CACR-14-06*, Center for Applied Coastal
775 Research, Department of Civil and Environmental Engineering, University of Delaware,
776 available at <http://www.udel.edu/kirby/papers/derakhti-kirby-cacr-14-06.pdf>.

777 Derakhti, M., and J. T. Kirby (2016), Breaking-onset, energy and momentum flux in un-
778 steady focused wave packets, *J. Fluid Mech.*, 790, 553–581, doi:10.1017/jfm.2016.17.

779 Derakhti, M., J. T. Kirby, F. Shi, and G. Ma (2015), NHWAVE: Model revisions and tests
780 of wave breaking in shallow and deep water, *Tech. rep.*, CACR-14-18, Center for Applied
781 Coastal Research, Dept. of Civil & Environmental Engineering, University of Delaware.

782 Derakhti, M., J. T. Kirby, F. Shi, and G. Ma (2016a), NHWAVE: Consistent boundary con-
783 ditions and turbulence modeling, *Ocean Modelling*, 106, 121–130, doi:10.1016/j.ocemod.
784 2016.09.002.

785 Derakhti, M., J. T. Kirby, F. Shi, and G. Ma (2016b), Wave breaking in the surf zone and
786 deep-water in a non-hydrostatic RANS model. Part 1: Organized wave motions, *Ocean*
787 *Modelling*, 107, 125–138, doi:10.1016/j.ocemod.2016.09.001.

788 Derakhti, M., J. T. Kirby, F. Shi, and G. Ma (2016c), Wave breaking in the surf zone and
789 deep-water in a non-hydrostatic RANS model. Part 2: Turbulence and mean circulation,
790 *Ocean Modelling*, 107, 139–150, doi:10.1016/j.ocemod.2016.09.011.

791 Derakhti, M., M. L. Banner, and J. T. Kirby (2018), Predicting the breaking strength of grav-
792 ity water waves in deep and intermediate depth, *J. Fluid Mech.*, 848, R2.

793 Dommermuth, D. G., and D. K. P. Yue (1987), A high-order spectral method for the study
794 of nonlinear gravity waves, *Journal of Fluid Mechanics*, 184, 267–288, doi:10.1017/
795 S002211208700288X.

796 Fedele, F., C. Chandre, and M. Farazmand (2016), Kinematics of fluid particles on the sea
797 surface: Hamiltonian theory, *J. Fluid Mech.*, 801, 260–288, doi:10.1017/jfm.2016.453.

798 Francois, M. M., S. J. Cummins, E. D. Dendy, D. B. Kothe, J. M. Sicilian, and M. W.
799 Williams (2006), A balanced-force algorithm for continuous and sharp interfacial surface
800 tension models within a volume tracking framework, *J. Comput. Phys.*, 213, 141–173.

801 Grilli, S. T., and R. Subramanya (1996), Numerical modeling of wave breaking induced by
802 fixed or moving boundaries, *Computational Mechanics*, 17(6), 374–391.

803 Grilli, S. T., J. Skourup, and I. A. Svendsen (1989), An efficient boundary element method
804 for nonlinear water waves, *Engineering Analysis with Boundary Elements*, 6(2), 97–107.

805 Grilli, S. T., R. Subramanya, I. A. Svendsen, and J. Veeramony (1994a), Shoaling of solitary
806 waves on plane beaches, *Journal of Waterway, Port, Coastal, and Ocean Engineering*,
807 120(6), 609–628.

808 Grilli, S. T., M. A. Losada, and F. Martin (1994b), Characteristics of solitary wave breaking
809 induced by breakwaters, *Journal of Waterway, Port, Coastal, and Ocean Engineering*,
810 120(1), 74–92.

811 Grilli, S. T., I. A. Svendsen, and R. Subramanya (1997), Breaking criterion and character-
812 istics for solitary waves on slopes, *Journal of Waterway, Port, Coastal, and Ocean Engi-
813 neering*, 123(3), 102–112.

814 Grilli, S. T., J. Horrillo, and S. Guignard (2019), Fully nonlinear potential flow simulations
815 of wave shoaling over slopes: Spilling breaker model and integral wave properties, *Water
816 Waves*, pp. 1–35, doi:doi:10.1007/s42286-019-00017-6.

817 Guignard, S., S. T. Grilli, et al. (2001), Modeling of wave shoaling in a 2d-nwt using a
818 spilling breaker model, in *The Eleventh International Offshore and Polar Engineering
819 Conference*, International Society of Offshore and Polar Engineers.

820 Guyenne, P., and S. Grilli (2006), Numerical study of three-dimensional overturning waves
821 in shallow water, *Journal of Fluid Mechanics*, 547, 361–388.

822 Iribarren, C. R., and C. Nogales (1949), Protection des ports, in *17th International Naviga-
823 tion Congress*, vol. 2, pp. 31–80.

824 Kennedy, A. B., Q. Chen, J. T. Kirby, and R. A. Dalrymple (2000), Boussinesq modeling of
825 wave transformation, breaking and runup. i: 1d, *Journal of Waterway, Port, Coastal and
826 Ocean Engineering*, 126(1), 39–47.

827 Khait, A., and L. Shemer (2018), On the kinematic criterion for the inception of breaking in
828 surface gravity waves: Fully nonlinear numerical simulations and experimental verifica-
829 tion, *Phys. Fluids*, 30(5), 057,103, doi:10.1063/1.5026394.

830 Kirby, J. T. (1998), Discussion of 'Note on a nonlinearity parameter of surface waves' by S.
831 Beji, *Coastal Engineering*, 34, 163–168.

832 Kirby, J. T. (2020), Low-order Boussinesq models based on σ coordinate series expansions,
833 *Journal of Fluid Mechanics*, (submitted).

834 Lakehal, D., and P. Liovic (2011), Turbulence structure and interaction with steep breaking
835 waves, *Journal of Fluid Mechanics*, 674, 522–577, doi:10.1017/jfm.2011.3.

836 Lin, P., and P. L. F. Liu (1999), Internal wavemaker for Navier-Stokes equations models,
837 *Journal of Waterway, Port, Coastal and Ocean Engineering*, 125(4), 207–215.

838 Luth, H., G. Klopman, and N. Kitou (1994), Kinematics of waves breaking partially on an
 839 offshore bar; ldv measurements of waves with and without a net onshore current, *Tech.
 840 rep.*, Delft Hydraulics, Report H-1573, 40 pp.

841 Ma, G., F. Shi, and J. T. Kirby (2011), A polydisperse two-fluid model for surf zone bubble
 842 simulation, *Journal of Geophysical Research*, 116(C05010), doi:10.1029/2010JC006667.

843 Mase, H., and J. T. Kirby (1992), Hybrid frequency-domain KdV equation for random wave
 844 transformation, in *Coastal Engineering 1992. Proceedings of the International Conference
 845 on Coastal Engineering*, pp. 474–487, ASCE, doi:10.1061/9780872629332.035.

846 McCowan, J. (1894), On the highest waves of a permanent type, *Philosophical Magazine,
 847 Edinburgh*, 38, 351–358.

848 Melville, W. K. (1996), The role of surface-wave breaking in air-sea interaction, *Annual Re-
 849 view Fluid Mech.*, 28, 279–321.

850 Miche, R. (1944), Breaking wave motion in water of constant depth, *Annales des Ponts et
 851 Chaussees*, 121, 285–319 (in French).

852 Mivehchi, A. (2018), Experimental and numerical simulations for fluid body interaction
 853 problems, Ph.D. thesis, University of Rhode Island, Narragansett, RI.

854 Papoutsellis, C. E., M. L. Yates, B. Simon, and M. Benoit (2019), Modelling of depth-
 855 induced wave breaking in a fully nonlinear free-surface potential flow model, *Coastal En-
 856 gineering*, 154, 103,579.

857 Perlin, M., W. Choi, and Z. Tian (2013), Breaking waves in deep and intermediate waters,
 858 *Annual Review Fluid Mech.*, 45, 115–145.

859 Pizzo, N., and W. K. Melville (2019), Focusing deep-water surface gravity wave packets:
 860 wave breaking criteria in a simplified model, *Journal of Fluid Mechanics*, 873, 238–259,
 861 doi:10.1017/jfm.2019.428.

862 Rapp, R. J., and W. K. Melville (1990), Laboratory measurements of deep-water breaking
 863 waves, *Philosophical Transactions of the Royal Society A*, 331, 735–800.

864 Raubenheimer, B., R. Guza, and S. Elgar (1996), Wave transformation across the inner surf
 865 zone, *J Geophys. Res.: Oceans*, 101, 25,589–25,597, doi:10.1029/96JC02433.

866 Robertson, B., K. Hall, R. Zytner, and I. Nistor (2013), Breaking waves: Review of character-
 867 istic relationships, *Coastal Eng. Journal*, 55(01), 1350,002.

868 Saket, A., W. L. Peirson, M. L. Banner, X. Barthelemy, and M. J. Allis (2017), On the thresh-
 869 old for wave breaking of two-dimensional deep water wave groups in the absence and
 870 presence of wind, *J. Fluid Mech.*, 811, 642–658, doi:10.1017/jfm.2016.776.

871 Saket, A., W. L. Peirson, M. L. Banner, and M. J. Allis (2018), On the influence of wave
 872 breaking on the height limits of two-dimensional wave groups propagating in uniform in-
 873 termediate depth water, *Coastal Eng.*, 133, 159–165.

874 Schäffer, H. A., P. A. Madsen, and R. Deigaard (1993), A boussinesq model for waves break-
 875 ing in shallow water, *Coastal Engineering*, 20, 185–202.

876 Schwendeman, M., and J. Thomson (2017), Sharp-crested breaking surface waves observed
 877 from a ship-based stereo video system, *Journal of Physical Oceanography*, 47, 775–792,
 878 doi:10.1175/JPO-D-16-0187.1.

879 Seiffert, B. R., and G. Ducrozet (2018), Simulation of breaking waves using the high-order
 880 spectral method with laboratory experiments: wave-breaking energy dissipation, *Ocean*
 881 *Dynamics*, 68, 65–89, doi:10.1007/s10236-017-1119-3.

882 Shemer, L., and D. Liberzon (2014), Lagrangian kinematics of steep waves up to the incep-
 883 tion of a spilling breaker, *Phys. Fluids*, 26(1), 016,601, doi:10.1063/1.4860235.

884 Song, J.-B., and M. L. Banner (2002), On determining the onset of and strength of break-
 885 ing for deep water waves. part i: Unforced irrotational wave groups, *Journal of Physical*
 886 *Oceanography*, 32, 2541–2558.

887 Stansell, P., and C. MacFarlane (2002), Experimental investigation of wave breaking criteria
 888 based on wave phase speeds, *Journal of physical oceanography*, 32(5), 1269–1283.

889 Tanaka, M. (1986), The stability of solitary waves, *The Physics of fluids*, 29(3), 650–655.

890 Tang, S., Z. Yang, C. Liu, Y.-H. Dong, and L. Shen (2017), Numerical study on the genera-
 891 tion and transport of spume droplets in wind over breaking waves, *Atmosphere*, 8, 248.

892 Tian, Z., M. Perlin, and W. Choi (2008), Evaluation of a deep-water wave breaking criterion,
 893 *Phys. Fluids*, 20, 066,604.

894 Ting, F. C. K., and J. T. Kirby (1994), Observations of undertow and turbulence in a labora-
 895 tory surf zone, *Coastal Engineering*, 24, 51–80.

896 Ting, F. C. K., and J. R. Nelson (2011), Laboratory measurements of large-scale near-bed
 897 turbulent flow strctures under spilling regular waves, *Coastal Engineering*, 58, 151–172,
 898 doi:10.1016/j.coastaleng.2010.09.004.

899 Toffoli, A., A. Babanin, M. Onorato, and T. Waseda (2010), Maximum steepness of oceanic
 900 waves: Field and laboratory experiments, *Geophys. Res. Lett.*, 37(5), doi:10.1029/
 901 2009GL041771.

902 Wei, G., J. T. Kirby, S. T. Grilli, and R. Subramanya (1995), A fully nonlinear boussinesq
 903 model for surface waves. part 1. highly nonlinear unsteady waves, *Journal of Fluid Me-*

904 *chanics*, 294, 71–92.

905 West, B. J., K. A. Brueckner, R. S. Janda, D. M. Milder, and R. L. Milton (1987), A new nu-
906 merical method for surface hydrodynamics, *Journal of Geophysical Research*, 92, 11,803
907 – 11,824, doi:10.1029/JC092iC11p11803.

908 Wiegel, R. L. (1960), A presentation of cnoidal wave theory for practical application, *J.*
909 *Fluid Mech.*, 7, 273–286.

910 Wu, C. H., and H. M. Nepf (2002), Breaking criteria and energy losses for three-dimensional
911 wave breaking, *Journal of Geophysical Research*, 107(C10), 3177, doi:10.1029/
912 2001JC001077.

913 Yang, Z., B.-Q. Deng, and L. Shen (2018), Direct numerical simulation of wind turbulence
914 over breaking waves, *J. Fluid Mech.*, 850, 120–155.